Real-Time Flight Simulation of Hydrobatic AUVs Over the Full 0°–360° Envelope

Sriharsha Bhat, *Member, IEEE*, Ivan Stenius, *Member, IEEE*, and Tianlei Miao, *Member, IEEE*

***Abstract*—Hydrobatic AUVs are very agile, and can perform challenging maneuvers that encompass the full 0°–360° flight envelope. Such AUVs can be beneficial in novel use cases in ocean production, environmental sensing, and security, by enabling new capabilities for docking, inspection, or under-ice operations. To further explore their capabilities in such scenarios, it is crucial to be able to model their flight dynamics over the full envelope, which includes strong nonlinear effects and turbulence at high angles of attack. With accurate and efficient simulation models, new hydrobatic maneuvers can be generated and control strategies can be developed. Therefore, this article contributes with a strategy to perform efficient and accurate simulations of hydrobatic maneuvers in real time. A multifidelity hydrodynamic database is synthesized by combining analytical, semiempirical, and numerical methods, thereby capturing fluid forces and moments over the full envelope. A component buildup workflow is used to assemble a nonlinear flight dynamics model using lookup tables generated from the database. This simulation model is used to perform real-time simulations of advanced hydrobatic maneuvers. Simulation results show agreement with literature and experiment, and the simulator shows utility as a development tool in designing new maneuvers and control strategies.**

***Index Terms*—Autonomous underwater vehicles, flight dynamics, flight simulation, hydrobatics, hydrodynamics, underactuated robotics.**

I. Introduction

THE term hydrobatics stems from aerobatics and refers to the agile maneuvering of underwater vehicles. Underactuated hydrobatic AUVs can be efficient (in terms of range and speed) and agile (in maneuvering), thereby offering potentially disruptive designs for application areas in ocean production, environmental sensing, and security [1]. The flight dynamics of such AUVs (especially during hydrobatic maneuvers) encompass the full $0^\circ - 360^\circ$ angle-of-attack (AoA) (α) envelope, far beyond the usual linearized, well-described region before stall. To further explore the capabilities of hydrobatic AUVs in specific use case scenarios (e.g., inspection, docking, and under-ice deployment), it is crucial to be able to model their flight dynamics over the full envelope. With accurate and efficient simulation models (see Fig. 1), new hydrobatic maneuvers can be generated and control strategies can be developed. Key requirements for such a simulation model include the following:

1) *accuracy* in representing flight dynamics and hydrodynamics over the full envelope with qualitatively realistic maneuvering;
2) *efficiency* in enabling real-time or close to real-time simulations (e.g., for controller design);
3) *applicability* of a simulator as a development tool with flexibility in changing configurations (e.g., rudder placement, thrusters, and internal trim systems).

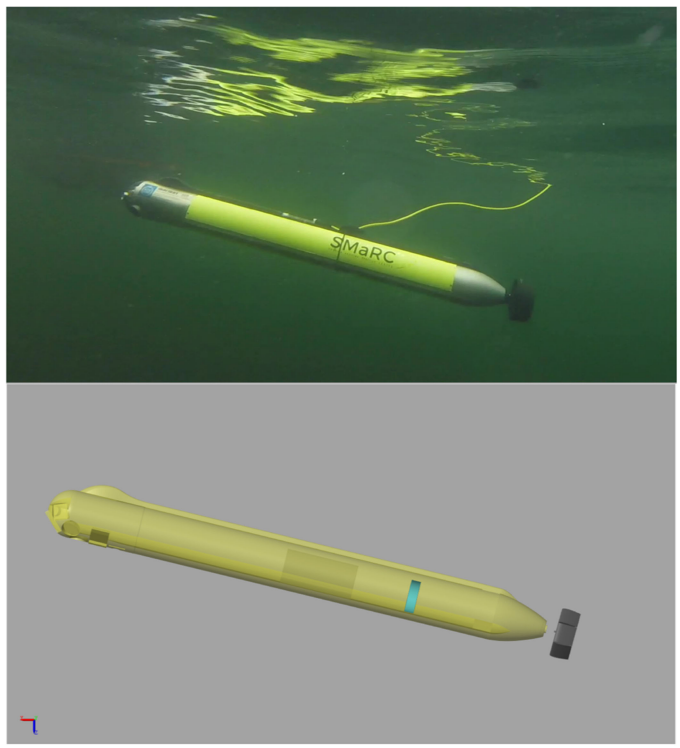

Fig. 1. Real-time AUV simulator can reflect real-world flight dynamics behavior and subsystems for generating hydrobatic maneuvers and tuning control strategies. Here, the hydrobatic SAM AUV is depicted, both in simulation and reality.

Manuscript received March 31, 2020; revised September 30, 2020 and February 11, 2021; accepted April 21, 2021. Date of publication July 6, 2021; date of current version October 13, 2021. This work was supported by the Swedish Foundation for Strategic Research (SSF) through the Swedish Maritime Robotics Centre (SMaRC) under Grant IRC15-0046. *(Corresponding author: Sriharsha Bhat.)*

Associate Editor: B. Englot.

Sriharsha Bhat and Ivan Stenius are with the School of Engineering Sciences, KTH Royal Institute of Technology, 10044 Stockholm, Sweden (e-mail: svbhat@kth.se; stenius@kth.se).

Tianlei Miao was with the KTH Royal Institute of Technology, 10044 Stockholm, Sweden. He is now with RH Marine, 3115 Schiedam, The Netherlands, and also with KU Leuven, 3000 Leuven, Belgium (e-mail: tianlei.miao@rhmarine.com).

This article has supplementary downloadable material available at https://doi.org/10.1109/JOE.2021.3076178, provided by the authors.

Digital Object Identifier 10.1109/JOE.2021.3076178

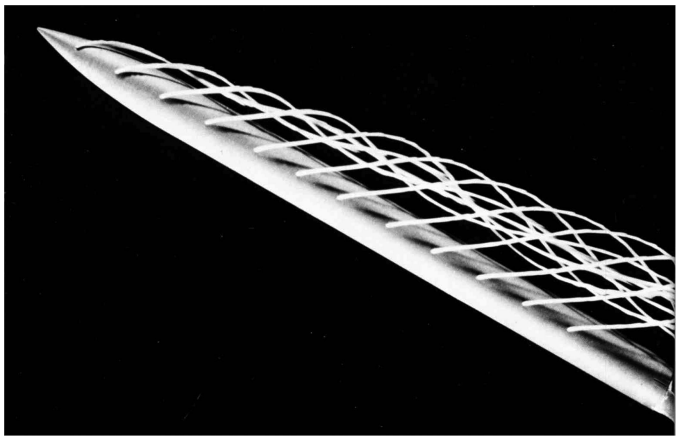

Fig. 2. Flow separation around a slender body at high angles of attack (from [13], reprinted in [14]).

With this motivation, the objective of this article is, therefore, to simulate hydrobatic AUVs in real time over the full flight envelope, thereby opening the doors to research on capabilities and applications. Such a simulation model would fit in well into a cyber-physical system where hydrobatic AUVs can be applied in real-world use cases [2], [3].

Flight simulation and hydrodynamic modeling of AUVs have been the focus of several publications including [4]–[9]. Fossen [4] and Healey and Lienard [5], in particular, offer comprehensive modeling frameworks for representing the equations of motion while allowing for the use of coefficients to represent the hydrodynamic forces and moments. Silva and Sousa [6] offer an interesting theoretical overview of modeling strategies and tradeoffs and Brutzman [7] describes an entire simulation environment. Prestero [9] applies the dynamics model in [5] to the Remus AUV, whereas Nahon [8] offers a simplified representation of the equations presented in [5]. However, the focus of the majority of literature has been on generalized representations to model the rigid body dynamics and the hydrodynamics together at low angles of attack below 15°. At higher incidence angles, the flow around the vehicle is transitional and turbulent—this leads to unsteady wakes around the body, meaning that traditional small-angle-of-attack results for the hydrodynamics may no longer be valid (see Fig. 2). Furthermore, the transition from laminar to turbulent flow and vice versa may occur at different angles of attack depending on the body, flow conditions, and hysteresis effects, thus adding to the complexity of the problem. Since most AUV operational scenarios do not require maneuvers at these angles, very few papers in the AUV literature explore this region.

Focusing on higher angles of attack, in [10], semiempirical data were interpolated for capturing unsteady regions to predict AUV performance for angles of attack up to 30°, whereas in [11], Jorgensen's analytical formulation [12] was used to calculate the AUVs hydrodynamics in the 0°–360° angle-of-attack range.

This article explores the problem of efficient and accurate flight simulations over the full 0°–360° angle-of-attack envelope with the following research contributions.

1) A *component build-up workflow* is proposed for efficiently modeling the flight dynamics for real-time simulations, building on the modeling representation presented by Fossen [4]. Precomputing lookup tables for component hydrodynamics and using a component buildup approach has the aim of simplifying and speeding up simulations without compromising quality. This workflow is applied to generate the Hydrobatics Simulator in Simulink.
2) A generalized framework is presented to model the hydrodynamic forces and moments over the full envelope, by assembling a *multifidelity hydrodynamic database* combining analytical/semiempirical and numerical/experimental methods. In this multifidelity approach, depending on what types of data are available, the database can be populated with different data sets in different flow regimes. This expands on the existing literature in [11] where only the analytical "Jorgensen's method" is used.
3) Based on the two points considered earlier, *real-time flight simulations* of several novel hydrobatic maneuvers are performed with the hydrobatic SAM AUV as a case study. A simulation model is generated in Simulink, and qualitatively validated with field experiments using a prototype AUV. The key contribution to existing methods is the ability to combine different data sets into a multifidelity framework where data from a variety of sources can be combined into a full $0^\circ - 360^\circ$ angle-of-attack range.

The subsequent sections are organized as follows. First, the theoretical aspects of flight dynamics modeling are described in the context of the component buildup approach with multifidelity lookup tables. Methods to populate the multifidelity database are then introduced, and the models and methods are combined to generate a real-time simulation framework. This framework is used to perform real-time simulations of hydrobatic maneuvers, and results of database validation, maneuvering and field tests are presented and discussed.

II. Flight Dynamics Modeling

In modeling the flight dynamics of hydrobatic AUVs, the key idea is to subcompose the robot into individual components, and to treat each component individually with its own dynamic properties. Once the individual components' dynamics are computed, they can be superposed to obtain the dynamics of the entire vehicle, thereby making the modeling flexible and efficient. This can generate a qualitatively accurate simulation model for the full flight envelope with close to real-time simulation [15].

The main challenge in modeling is in computing the fluid forces over the full flight envelope. The strategy used here is to generate a set of precalculated lookup tables of appropriate complexity for the hydrodynamics for a predefined flight envelope and for each component. This is schematically illustrated in Fig. 3. The full flight envelope is defined as a discrete range of Reynolds numbers, angles of attack (α) and side-slip angles (β). During simulation, for each component and flight condition, the corresponding hydrodynamic coefficients are obtained by interpolation between closest points, which are used to compute forces and moments. These lookup tables can be populated based

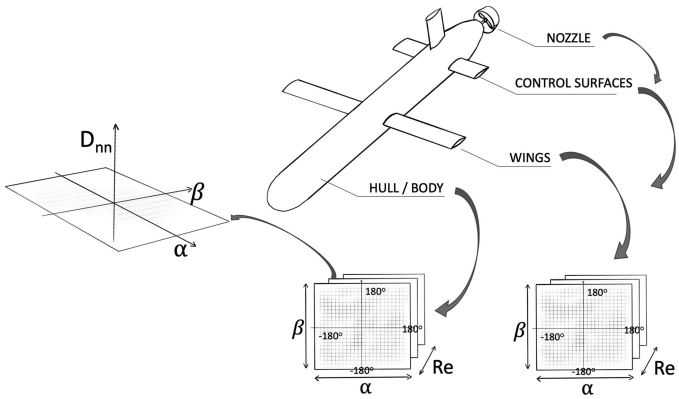

Fig. 3. Schematic illustration of lookup tables capturing the nonlinear hydrodynamic forces for each subcomponent over the full envelope.

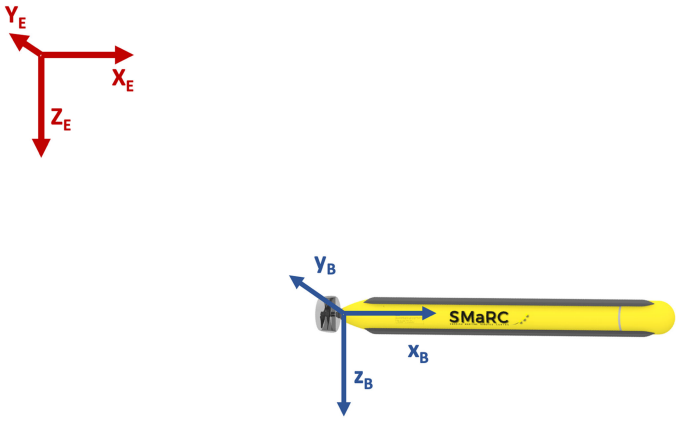

Fig. 4. Coordinate systems in the world and component frames used in modeling.

on the best available data for each flight condition, which implies a multifidelity modeling approach.

Building on the theoretical framework in [4], if a generalized multifidelity hydrodynamic model can be used to obtain detailed and accurate representations for each component over the full envelope, then a qualitatively accurate simulation model can be generated for close to real-time simulation. To perform such real-time flight simulations, it is necessary to solve the equations of motion represented by Newton's second law, together with accurate estimates/computations of the fluid forces and moments acting on each component. While integration of the motion equations is straightforward, computing the fluid dynamics is not; and combining the two is a challenge.

A. Kinematics

Unit quaternions enable kinematic modeling over the full $0^\circ - 360^\circ$ flight envelope for hydrobatic maneuvers. Quaternions are used to represent orientations instead of the traditional Euler angles to prevent a singularity at 90° pitch angle [6]. The global coordinate system used as the world frame is the SNAME NED [16] frame, with the downward Z-axis being positive. Locally, in each component frame, a body-fixed right hand Cartesian coordinate system is used (see Fig. 4).

The positions and orientations in the world frame are combined as the pose vector $\boldsymbol{\eta} = [x_E\ y_E\ z_E\ \eta\ \varepsilon_1\ \varepsilon_2\ \varepsilon_3]^T$. Here, $[x_E, y_E, z_E]$ represent the positions, and $[\eta, \varepsilon_1, \varepsilon_2, \varepsilon_3]$ are unit quaternions representing the rotations. Quaternion rotations can easily be converted to Euler angles and vice versa.

The linear and angular velocities are combined in the velocity vector $\boldsymbol{\nu} = [u\ v\ w\ p\ q\ r]^T$, where $[u, v, w]$ are the translational velocities and $[p, q, r]$ are the rotational velocities with respect to the x_B, y_B, and z_B axes in the body fixed frame. The kinematics of the AUV in six degrees of freedom are represented in vector form as

$$\dot{\boldsymbol{\eta}} = \mathbf{J}_q(\boldsymbol{\eta})\boldsymbol{\nu} \tag{1}$$

where $\mathbf{J_q} \in \mathbb{R}^{7\times 6}$ is a combined transformation matrix given by

$$\mathbf{J_q}(\boldsymbol{\eta}) = \begin{bmatrix} \mathbf{T_q} & \mathbf{0}_{3\times 3} \\ \mathbf{0}_{4\times 3} & \mathbf{R_q} \end{bmatrix} \tag{2}$$

and the translational transformation matrix $\mathbf{T_q} \in \mathbb{R}^{3\times 3}$ and rotational transformation matrix $\mathbf{R_q} \in \mathbb{R}^{4\times 3}$ are given by

$$\mathbf{T_q} = \frac{1}{2}\begin{bmatrix} 1-2(\varepsilon_2^2+\varepsilon_3^2) & 2(\varepsilon_1\varepsilon_2-\varepsilon_3\eta) & 2(\varepsilon_1\varepsilon_3+\varepsilon_2\eta) \\ 2(\varepsilon_1\varepsilon_2+\varepsilon_3\eta) & 1-2(\varepsilon_1^2+\varepsilon_3^2) & 2(\varepsilon_2\varepsilon_3-\varepsilon_1\eta) \\ 2(\varepsilon_1\varepsilon_3-\varepsilon_2\eta) & 2(\varepsilon_2\varepsilon_3+\varepsilon_1\eta) & 1-2(\varepsilon_1^2+\varepsilon_2^2) \end{bmatrix} \tag{3}$$

and

$$\mathbf{R_q} = \begin{bmatrix} -\varepsilon_1 & -\varepsilon_2 & -\varepsilon_3 \\ \eta & -\varepsilon_3 & \varepsilon_2 \\ \varepsilon_3 & \eta & -\varepsilon_1 \\ -\varepsilon_2 & \varepsilon_1 & \eta \end{bmatrix}. \tag{4}$$

B. Dynamics

The key idea in modeling the dynamics is to utilize generalized representations of hydrodynamic damping, thereby capturing nonlinear effects over the full envelope. A vectorial robotlike representation as presented by Fossen in [4] can be used to describe the dynamics of each AUV component as a virtual spring–mass–damper system

$$\begin{aligned} &\boldsymbol{M}_{RB}\dot{\nu} + C_{RB}(\nu)\nu + M_A\dot{\nu} + C_A(\nu)\nu + D(\nu)\nu \\ &\quad + g(\boldsymbol{\eta}) = \tau_C \end{aligned} \tag{5}$$

where $\mathbf{M_{RB}}$ is the rigid body mass and inertia matrix and $\mathbf{C_{RB}}$ is the matrix of Coriolis and centripetal terms on the left-hand side. $\boldsymbol{M_A}$ and $\boldsymbol{C_A}(\nu)$ represent the effect of added mass, $\boldsymbol{D}(\nu)$ represents the damping matrix and $\boldsymbol{g}(\eta)$ is the vector of gravitational and buoyancy forces and moments. $\boldsymbol{\tau_C} = [X_C\ Y_C\ Z_C\ K_C\ M_C\ N_C]^T$ is a vector of external control forces, which depends on each specific robot's actuator configuration.

The $\mathbf{M_{RB}}$ and $\mathbf{C_{RB}}$ matrices can be easily calculated if the component mass m, inertia tensor $I_0 \in \mathbb{R}^{3\times 3}$ and center-of-gravity (c.g.) position $\boldsymbol{r_g} = [x_G\ y_G\ z_G]^T$ are known. The hydrostatic forces and moments in $\boldsymbol{g}(\boldsymbol{\eta})$ can be calculated based on weight, geometry, and orientation using Archimedes' principle. The key challenge (as also pointed out in [17]) is to

obtain an accurate estimate of the damping terms. This becomes particularly difficult for large angles of attack where the solution is affected by strong nonlinear effects. A generalized framework for handling the hydrodynamic damping coefficients for the full flight envelope can be beneficial so that the hydrodynamic forces can be calculated efficiently during simulations. The same approach can later be translated for the added mass and inertia matrices as well.

The damping matrix $\boldsymbol{D}(\nu)$ can be a combination of linear and nonlinear damping terms. Several simplifications are usually made considering decoupled modes and symmetry considerations (see [17]) restricting it to a constrained set of DOFs and angles of attack based on the operational region. However, for hydrobatic maneuvering, such simplifications are not desirable and it is essential to be able to simulate complex motions and couplings in the full flight envelope and 6 DOF. Such a generalized representation of $\boldsymbol{D}(\nu)$ without any simplifying assumptions, considering all couplings and including linear and nonlinear effects is given by

$$\mathbf{D}(\boldsymbol{\nu}) = \begin{bmatrix} D_{11} & D_{12} & D_{13} & D_{14} & D_{15} & D_{16} \\ D_{21} & D_{22} & D_{23} & D_{24} & D_{25} & D_{26} \\ D_{31} & D_{32} & D_{33} & D_{34} & D_{35} & D_{36} \\ D_{41} & D_{42} & D_{43} & D_{44} & D_{45} & D_{46} \\ D_{51} & D_{52} & D_{53} & D_{54} & D_{55} & D_{56} \\ D_{61} & D_{62} & D_{63} & D_{64} & D_{65} & D_{66} \end{bmatrix}. \quad (6)$$

The terms D_{nn} may be anything from simple linear uncoupled hydrodynamic terms to fully coupled higher order nonlinear coefficients—an appropriate set of hydrodynamic coefficients, given the chosen level of complexity for the hydrodynamic modeling must be considered. The most common notation to populate the D_{nn} terms is to use hydrodynamic derivatives. Each derivative is the partial derivative of the hydrodynamic force with respect to a particular variable. For linear hydrodynamic damping coefficients, this may, for example, be formulated as $X = X_u u$, where $X_u = \left(\frac{\partial X}{\partial u}\right)$. Following the same notation, nonlinear damping coefficients such as X_{uu}, Y_{vv}, and Z_{ww} can also be formulated. These coefficients are usually considered to be constant within a small operating region in the traditional literature. The use of lookup tables (as illustrated in Fig. 3) means they can instead be a nonlinear function of the flow condition, thereby capturing the essentially nonlinear behavior of the hydrodynamic forces over an extended region.

III. Multifidelity Hydrodynamic Database

To accurately represent the hydrodynamic damping (D_{nn}) terms in (6), the key idea is to populate the lookup tables with data based on the best available sources, which may vary for different flow conditions. For example, it is easy to obtain lift and drag coefficients for an arbitrary airfoil at laminar flow conditions; however, for poststall conditions, accurate data are much harder to obtain. Hence, at low angles of attack, the database may be built up from data with high fidelity, whereas for higher (poststall) angles of attack, the data may be less accurate. This forms a multifidelity database where the best available data are used to populate the database with data for the entire flight envelope. Such a multifidelity database provides a straightforward way of modeling advanced maneuvers for AUVs with relatively fast and simple simulation tools. The same approach can also be used for the added mass terms, but the focus here is on the hydrodynamic damping.

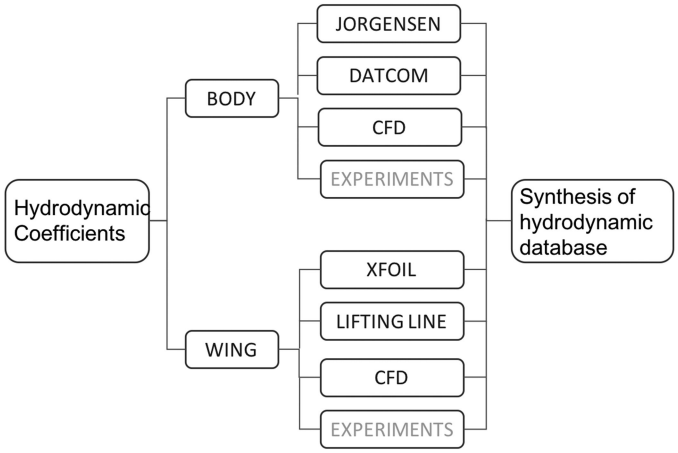

Fig. 5. Overview of methods combined within a multifidelity database.

There may be many sources for the data, in assembling such a multifidelity hydrodynamic database, typically coming from experiments, numerical methods, and analytic semiempirical approaches. Data are collected based on a range of Reynolds' numbers (Re) and angles of attack (α as well as side-slip angles β) and, then, selecting the highest fidelity data available at that flow condition. Combining different hydrodynamic data sets using this approach and obtaining the best available representations is a key challenge. On one hand, appropriate data needs to be selected for a specific flow condition; and on the other hand, a physically realistic database needs to be generated for the full flight envelope with smooth transitions between different data sets.

In this article, the proposed approach is based on two categories of hydrodynamic data sets – one for main hull bodies and one for control surfaces (see Fig. 5), which will be described next. More advanced components such as nozzles can be assembled from a number of smaller airfoil profiles while nonslender bodies can also be included if appropriate hydrodynamic data are available. In this section, five readily available methods for populating the full envelope database are considered, including the following.

1) *Jorgensen's method* [12], which offers an analytical formulation to compute the flow over the full envelope angle-of-attack range for slender bodies.
2) *DATCOM*, which includes a combination of analytical and semiempirical methods for subsonic bodies of revolution in [18]. This can be used to augment Jorgensen's formulation at low incidence angles.

3) *Computational fluid dynamics (CFD) methods*, which are powerful tools to provide a more accurate numerical solution at selected Reynolds' numbers and angles of attack (e.g., [19]).
4) Analytical methods for wings and airfoils such as the lifting line theory and potential flow over a flat plate.
5) *XFOIL* [20], which offers a rapid numerical solutions for low-Reynolds' number airfoils and wings at low angles of attack.

Properly conducted experimental determination of hydrodynamic derivatives is still the most accurate and reliable method (e.g., [21]). However, experiments are also typically very expensive and require access to a proper model as well as access to large and complex infrastructures such as towing tanks, wave basins and rotating-arm facilities. While such experiments are beyond the scope of this article, their results can be easily integrated into the database with the methodology presented.

A. Body (Main Hull)

1) Jorgensen's Method: In [12], Jorgensen presented a procedure for computing normal force, axial force, and pitching moment coefficients for slender bodies of circular and noncircular cross sections over the $0^\circ - 180^\circ$ angle-of-attack range. Jorgensen's method combines slender body potential flow theory together with viscous flow separation effects due to cross flow. While it was originally applied to study the aerodynamics of space-shuttle re-entry, the same method is used in [11], [22], and [23] to compute the hydrodynamic coefficients for slender flight style AUVs, at high angles of attack.

The normal force coefficients over $0^\circ \leq \alpha \leq 180^\circ$ (where α is the angle of attack) are expressed as

$$C_N = (k_2 - k_1)\frac{A_b}{A}\sin(2\alpha')\cos\left(\frac{\alpha'}{2}\right) + \eta C_{d_n}\frac{A_p}{A}\sin^2(\alpha') \tag{7}$$

where the first term represents potential flow, and the second accounts for viscous flow separation effects due to cross flow and

$$\alpha' = \alpha, \qquad \text{for} \quad 0^\circ \leq \alpha \leq 90^\circ$$
$$\alpha' = 180^\circ - \alpha, \qquad \text{for} \quad 90^\circ \leq \alpha \leq 180^\circ.$$

Similarly, expressions for axial force and pitching moment coefficients for $0^\circ \leq \alpha \leq 90^\circ$ are

$$C_A = C_{A_{\alpha=0^\circ}}\cos^2(\alpha') \tag{8}$$

and

$$C_M = \left[(k_2 - k_1)\frac{V - A_b(L - x_m)}{AL}\right]\sin(2\alpha')\cos\left(\frac{\alpha'}{2}\right) + \eta C_{d_n}\frac{A_p}{A}\left(\frac{x_m - x_c}{L}\right)\sin^2(\alpha'). \tag{9}$$

The same expressions for $90^\circ \leq \alpha 180^\circ$ are presented as

$$C_A = C_{A_{\alpha=180^\circ}}\cos^2(\alpha') \tag{10}$$

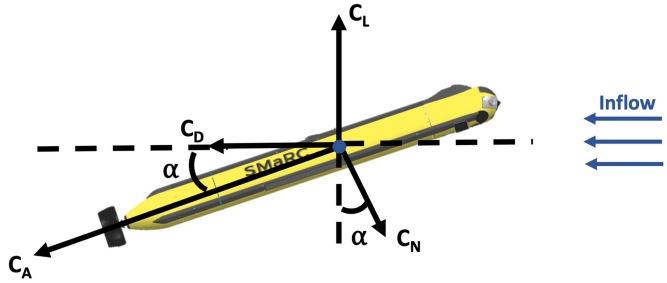

Fig. 6. Axial and normal forces in the longitudinal plane (for Jorgensen's method and DATCOM).

$$C_M = -\left[(k_2 - k_1)\frac{V - A_b(L - x_m)}{AL}\right]\sin(2\alpha')\cos\left(\frac{\alpha'}{2}\right) + \eta C_{d_n}\frac{A_p}{A}\left(\frac{x_m - x_c}{L}\right)\sin^2(\alpha'). \tag{11}$$

Here, C_A, C_N, and C_M are the axial, normal, and pitching moment coefficients, respectively; $C_{A_{\alpha=0^\circ}}$ and $C_{A_{\alpha=180^\circ}}$ are the form drag coefficients of the hull at an angle of attack 0° and 180°, respectively; V is the hull volume; L is the reference length; k_2 and k_1 are Munk moment coefficients; A_b is the cross-sectional base area of the hull; x_m is the distance from nose to the pitching moment center, A is the reference area; η is the cross-flow drag proportionality factor (ratio of the cross-flow drag coefficient for a finite-length cylinder to that of an infinite-length cylinder; C_{d_n} is the cross-flow drag coefficient of a circular cylinder, A_p is the planform area of the hull, and x_p is the distance from the nose to the centroid of the planform area of the hull; α is the hull angle of attack (seen in Fig. 6). C_N and C_A are transformed to C_L and C_D by projecting them to the relevant flow oriented frames. A simple transformation of coordinates can be used to also translate the coefficients for the $(-180^\circ - 0^\circ)$ region as well.

2) DATCOM: The United States Air Force Stability and Control DATCOM (short for Data Compendium) is a collection of aerodynamic prediction methods for aircraft, and is intended to offer a full set of preliminary aerodynamic data before any tests are conducted [18]. DATCOM can also be applied to AUVs if appropriate similitude is performed [24]. In this article, methods for bodies in subsonic flow at different angles of attack (available in [18, Sec. 4.2]) are selected and utilized.

First, the lift coefficient C_L is considered. For low angles of attack up to 12°, a calculation method from Hopkins [25] is recommended, which considers potential flow and viscous effects from cross-flow drag as

$$C_L = \frac{(k_2 - k_1)2\alpha S_o}{V_B^{2/3}} + \frac{2\alpha^2}{V_B^{2/3}}\int_{x_o}^{l_B}\eta r c_{d_c}\, dx \tag{12}$$

where k_2 and k_1 are the Munk moment factors, α is the angle of attack, S_0 is the cross-sectional area where the flow ceases to be potential at the point x_0 (i.e., where $\left(\frac{dS_x}{dx}\right)$ reaches its maximum negative value), V_B is the body volume, η is the ratio of the drag on a finite cylinder to the drag on an infinite cylinder,

r is the body radius at any longitudinal station, c_{d_c} is the steady-state cross-flow drag coefficient of a circular cylinder of infinite length, and l_B is the body length.

At higher angles of attack from 12° to 180°, Jorgensen's method is used. The Munk moment term $(k_2 - k_1)$ can be set to 1 at high fineness ratios (l/d). Considering the drag coefficient C_D, the total drag of a body at angle of attack can be expressed as a combination of zero lift drag C_{D_0} and drag due to angle of attack $C_D(\alpha)$ as

$$C_D = C_{D_0} + C_D(\alpha)\ . \tag{13}$$

C_{D_0} is expressed as a combination of the turbulent flat-plate skin-friction drag coefficient C_{d_f}, and the body coefficient is based on the frontal area C_{D_b}, giving

$$C_{D_0} = C_{D_f} + C_{D_b}\ . \tag{14}$$

C_{D_f} is computed from the turbulent flat-plate skin-friction coefficient based on the reference length (see [18, Fig. 4.1.5]) according to

$$C_{D_f} = C_f \left[1 + \frac{60}{\left(\frac{l_B}{d}\right)^3} + 0.0025\left(\frac{l_B}{d}\right)\right]\frac{S_S}{S_B} \tag{15}$$

while C_{d_b} is calculated according to

$$C_{D_b} = \frac{0.029\left(\frac{d_b}{d}\right)^3}{\sqrt{(C_{D_f})_b}}\ . \tag{16}$$

At angles of attack up to 15°, a high fineness ratio empirical method is used to compute $C_D(\alpha)$, which offers validity for $l/d > 6$. The drag coefficient is given by

$$C_D(\alpha) = \frac{2\,A}{V_B^{2/3}}2\alpha^2 + \eta C_{d_n}\frac{A_p}{V_B^{2/3}}\alpha^3 \tag{17}$$

where A is the wetted surface area and A_p is the planform area, and the other variables are the same as described in (12). At higher angles of attack from 15° to 180°, Jorgensen's method is used, just like in the case of the lift coefficient, but with refined definitions of axial force coefficient at 0° and 180° according to

$$\begin{aligned} C_{A_{\alpha=0^\circ}} &= -(C_f + C_{D_b}) \\ C_{A_{\alpha=180^\circ}} &= C_f + C_{D_b}. \end{aligned} \tag{18}$$

Finally, the moment coefficient C_M is considered. At angles of attack up to 12°, slender body theory is used giving

$$C_M = 2\left(\frac{x_m}{l_b} + \frac{V_B}{Al_b} - 1\right)\alpha \tag{19}$$

while at higher angles of attack $12^\circ - 180^\circ$, Jorgensen's method is used once more.

The methods used from the compendium in [18] for computing C_L, C_D, and C_M over the full envelope are summarized in Table I. Alternative methods, especially at low angles of attack and for nonslender bodies are also presented for all three coefficients in [18], and these can be employed if necessary.

3) Computational Fluid Dynamics: CFD methods involve numerical solutions to the Navier–Stokes (N-S) equations under specific conditions. These methods enable an accurate evaluation of the magnitude of the hydrodynamic forces [26], but at a high computational cost. CFD calculations can be employed to provide higher fidelity snapshots of the flow around a body at certain operating points, thus offering a high fidelity method in critical regions (both for the validation of simpler methods and to improve accuracy). CFD can be used to calculate the drag (C_D), lift (C_L), and moment (C_M) coefficients for an AUV body (e.g., [19]), and it is possible to compute flow coefficients at selected Reynolds' numbers over the full envelope. However, an appropriate mesh, solver, and turbulence model is critical for a valid and reliable problem setup.

Furthermore, virtual experimental tests can also be generated, and used to compute hydrodynamic derivatives, as described in [21]. In all cases, it is crucial to ensure similitude by scaling reference values when mixing data sources. It is also possible to solve the N-S and rigid body dynamics equations together using coupled solvers, but such an approach is not yet real-time valid and even if it were, it would most likely be very expensive computationally [6].

Considering the aerospace domain, CFD has been used to compute the flow around an aircraft at varying angles of attack, and curve-fitting or kriging has been used to generate aerodynamic lookup tables for flight simulation from CFD results [27]. As a next step, automated CFD with multifidelity methods has also been proposed for aerodynamic data over the full envelope [28].

TABLE I
SUMMARY OF RELEVANT METHODS FROM DATCOM

Coefficients	*AoA(degree)*	*Methods*
C_L	0-12	Potential flow combined with viscous flow separation effects [25]
	12-180	Jorgensen's method [12]
C_D	0-15	High fineness ratio empirical method [18]
	15-180	Jorgensen's method [12]
C_M	0-12	Slender body theory [18]
	12-180	Jorgensen's method [12]

B. Wings (Rudders, Fins, Wings, etc.)

1) Lanchester–Prandtl's Lifting Line Theory: For incompressible and inviscid flows a simple solution to lift and drag on 3-D wings can be obtained from Lanchester–Prandtl's lifting line model [29]. The lift force is calculated from the lift coefficient

$$C_L = \frac{C_l}{1 + \dfrac{2}{e\mathrm{AR}}} \tag{20}$$

where C_l is the two-dimensional lift coefficient, AR is the wing effective aspect ratio, and e is the so-called Oswald's span efficiency factor. The drag / resistance of the wing in 3-D is affected by a so-called lift induced drag CDi (or short "induced drag") since it only exists when lift is generated. This induced

drag coefficient is formulated as

$$C_{Di} = \frac{C_L^2}{\pi e \mathrm{AR}} . \tag{21}$$

This leads to the total drag of a 3-D lifting wing, as the sum of its profile drag C_{D0} (often called parasite drag taken at $\alpha = 0$) and the induced drag C_{Di}

$$C_D = C_{D0} + C_{Di} . \tag{22}$$

Furthermore, a pitching moment acts on asymmetrical wings and wings at an angle of attack. This is usually formulated in terms of a center of pressure x_{cp} position or a pitching moment coefficient C_M acting on the wing. Equations (20) and (22) may be good approximations at lower angles of attack, but beyond stall, at higher angles of attack, there is no simple expression with reasonable accuracy. A flat-plate assumption may be made to obtain the full flight envelope in a simple manner. However, the accuracy of this approach is limited; so, it is also important to combine different data sets for wings.

A method proposed by Montgomerie in [30] can be used to interpolate between potential flow calculations at low angles of attack, and flow over a flat plate at high angles of attack above stall. A linear interpolation is, then, performed to reduce discontinuities in the transition region. The use of Montgomerie's interpolant makes it possible to have a smooth transition between different data sets for wings.

2) XFOIL: XFOIL is an analysis tool for airfoils, wings, and aircraft at low Reynolds' numbers [20]. At low angles of attack, XFOIL can be used to cross validate and augment analytical calculations for wings. Within XFOIL, lift and drag forces (as well as moments) can be computed using lifting line theory or on the vortex lattice method, and the region of first flow separation at stall can be captured.

IV. Real-Time Simulation

A. Simulation Workflow

Efficient and accurate real-time simulations can be performed by bringing together full envelope hydrodynamic models of the different AUV components using the component build-up method. Using this idea, the simulation environment of the Hydrobatics Simulator is built up using software packages from Mathworks[1] (MATLAB and Simulink), with the following workflow.

1) All the AUV component geometries are imported as CAD stereolithography (.stl) files.
2) Model parameters such as mass, inertia, and center-of-gravity position are specified by the user while others such as volume, center of buoyancy, and geometric parameters such as width, height, wetted surfaces, cross sections, etc., are computed from the CAD models.
3) For all subcomponents in an assembly, *full envelope hydrodynamic databases* are synthesized as lookup tables for a predefined range of Reynolds' numbers (Re).

[1]Online. [Available]: https://se.mathworks.com

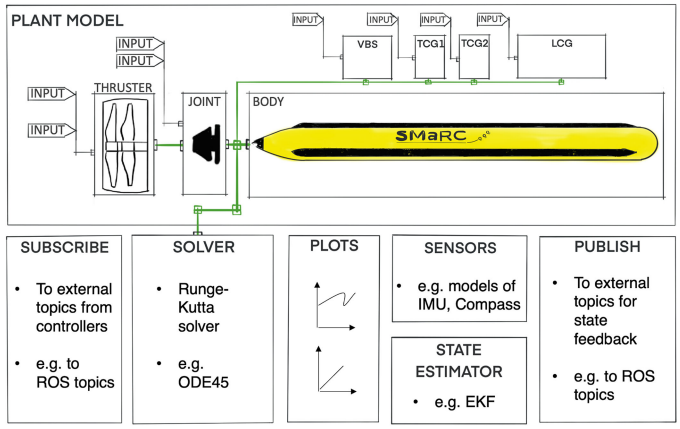

Fig. 7. Flight simulation framework in Simulink including models of components and actuator within the plant model. Other functions within the framework include a publish/subscribe architecture, solvers, plots, sensors, and estimator models.

A multifidelity approach is used where, depending on what type of data are available, the database can be populated with different data sets in different flow regimes. This is intended to simplify and speed up the simulation without compromising quality.

4) The *flight dynamics model* is assembled in Simulink, including frames, components and subsystems (see example layout in Fig. 7). The coordinate transformations between the world frame and local component frames are managed by Simscape, which enables kinematic representations using quaternions. The steps to assemble a model include the following:
   a) setup of world frame, solver and vehicle frame;
   b) assemble components and actuator subsystems;
   c) specify locations and constraints of component frames.
5) Initial conditions are defined (position, orientation, and velocities) and time stepping is performed to simulate the dynamics of the AUV for specific maneuvers (e.g., using a Runge–Kutta solver in Simulink). The following computations take place at each time step.
   a) Compute hydrostatic forces based on the geometry.
   b) Compute hydrodynamic forces based on database lookup tables. The forces and moments acting on each component are individually calculated in their individual body-fixed reference frames. These are then added up in a world frame, where the motion of the entire vehicle is calculated and observed.
   c) Compute external forces (such as thrusters).
   d) Include changes to state variables from actuators.
6) Postprocessing is performed.

The method is general and any AUV can be simulated using this workflow if the hydrodynamics are sufficiently well defined. The workflow is applied to SMaRCs SAM AUV, a slender torpedo-shaped underactuated AUV as a case study in Section V.

While the approach is relatively straightforward, it is to be noted that interactions between components are not accounted for, which may be significant in some cases (such as shadowing of control surfaces).

B. Database Assembly

Using the multifidelity approach presented in this article, a hydrodynamic database can be assembled for each component where the best available hydrodynamic data are used to estimate the hydrodynamic derivatives for the entire velocity range for $\alpha \in [-180^\circ, 180^\circ]$. Algorithms 1 and 2 provide example procedures for populating such a database.

Typically, at flow conditions where reliable experimental or CFD results are available, these results are prioritized. Within the range of Reynolds' numbers where higher fidelity results are available, DATCOM at low α and Jorgensen's method for higher α may also be used to fill in gaps in the data. Outside this range, DATCOM seems to give reasonable results and can be used unless more reliable data are available. A challenge is to combine the data sets with smooth transitions. In this article, this is achieved by interpolating between the discrete populated points using the *makima*[2] interpolation method (short for *Modified Akima piecewise cubic Hermite interpolation*). Algorithm 1 details the process in full.

Similarly, considering wings and control surfaces in Algorithm 2, an example approach in selecting the data sets is given here. As for the body case in Algorithm 1, whenever correct experimental or CFD based data sets are available, these should most likely be selected. Otherwise, at low α and Re, tools such as XFOIL may be used to compute lift and drag coefficients. The base computation here uses lifting line theory at low angles of attack ($\alpha \leq 10^\circ$) and flat plate theory at higher angles of attack, with the transition between the two methods according to the work in [30] for $\alpha = 10^\circ \rightarrow 15^\circ$.

Algorithm 1: Database Generation: Body.

Result: Body hydrodynamic database

for $Re \leftarrow 10^5$ **to** 10^7 **do**
  for $\alpha \leftarrow -180^\circ$ **to** 180° **do**
    if *Expt isAvailable()* **then**
      use Expt for $C_{L,D,M}(\alpha, Re)$;
    else if *CFD isAvailable()* **then**
      use CFD for $C_{L,D,M}(\alpha, Re)$;
    if *Re* $\leq$ *Threshold* **then**
      if $|\alpha| < 15^\circ$ **then**
        use DATCOM for $C_{L,D,M}(\alpha, Re)$;
      else if $15^\circ \leq |\alpha| \leq 180^\circ$ **then**
        use Jorgensen for $C_{L,D,M}(\alpha, Re)$;;
    else if *Re* $>$ *Threshold* **then**
      use DATCOM for $C_{L,D,M}(\alpha, Re)$;
  end
end
Interpolate $C_{L,D,M}$ using *makima* for a continuous surface;
Transform coordinates and dimensionalize.

Algorithm 2: Database Generation: Wings.

Result: Wing hydrodynamic database

Transform coordinates to component frame;
for $Re \leftarrow 10^4$ **to** 10^6 **do**
  for $\alpha \leftarrow -180^\circ$ **to** 180° **do**
    if *Expt isAvailable()* **then**
      use Expt for $C_{L,D,M}(\alpha, Re)$;
    else if *CFD isAvailable()* **then**
      use CFD;
    if $|\alpha| < 10^\circ$ **then**
      if *XFOIL isAvailable()* **then**
        use XFOIL for $C_{L,D,M}(\alpha, Re)$;
      else
        use Lifting Line for $C_{L,D,M}(\alpha, Re)$;
      end
    else if $10^\circ \leq |\alpha| \leq 180^\circ$ **then**
      use Flat Plate for $C_{L,D,M}(\alpha, Re)$;
  end
end
Interpolate $C_{L,D,M}$ for transition using Montgomerie's method [30];
Transform coordinates and dimensionalize.

V. Results: SAM AUV Case Study

The results section focuses on validation of the proposed multifidelity method. To begin, the reliability of the semiempirical hydrodynamic derivatives is checked by comparing with known data from the literature. Second, a multifidelity database is assembled for the SAM AUV, and the simulation validity is analyzed by pushing the simulations into high angle-of-attack regimes and hydrobatic maneuvers. Finally, a comparison is performed between the simulation results and real-world maneuvering experiments.

A. SAM AUV Modeling

The AUV SAM (see Fig. 1) with hydrobatic capabilities developed at the Swedish Maritime Robotics Center (see [3] and [31]) is here used to demonstrate simulations of advanced maneuvers by using the multifidelity approach.

1) Actuator Subsystems: SAM is around 1.5 m long and weighs around 15 kg. Hydrobatic capabilities are enabled by several actuator subsystems for control, as seen in Fig. 8. Counterrotating propellers are used for propulsion and a thrust vectoring subsystem is used for steering. In addition, the buoyancy of the vehicle can be controlled by a variable buoyancy subsystem (VBS); and the position of the center of gravity can be controlled using the longitudinal and transversal center of gravity (LCG and TCG) trim subsystems. The propulsion and thrust vectoring subsystems influence the control force vector $\boldsymbol{\tau_C}$. The trim and buoyancy subsystems influence the mass and the center-of-gravity position, thereby affecting the $\boldsymbol{M_{RB}}$ and $\boldsymbol{C_{RB}}$ matrices. Within the simulator, the VBS is modeled as

[2]Online. [Available]:https://se.mathworks.com/help/matlab/ref/makima.html

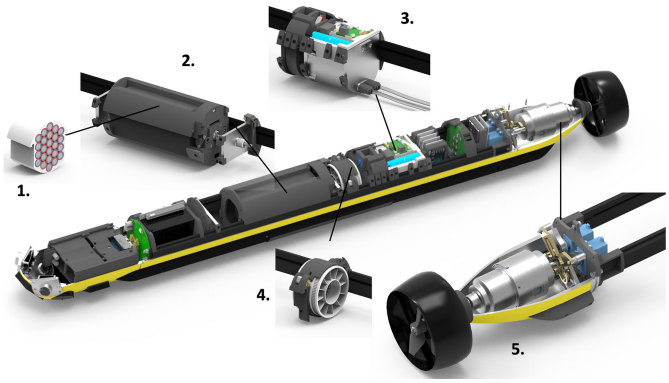

Fig. 8. Hardware subsystems on SAM modeled in the simulator. 1) Battery pack. 2) LCG trim. 3) Variable buoyancy system (VBS). 4) TCG trim. 5) Thrust vectoring and propulsion (picture courtesy: Josefine Severholt).

a variable mass cylinder (representing a piston), the LCG is modeled as a linearly moving mass and the TCG is modeled as two revolving masses.

2) Nonlinear Damping: Since the operating region includes high angles of attack, the damping behavior of SAM is highly nonlinear, and this is reflected in the damping matrix $\boldsymbol{D}(\boldsymbol{\nu})$,

The hydrodynamic damping forces $[\,X_D\ Y_D\ Z_D\,]^T$ are, therefore, modeled with nonlinear damping coefficients $\mathbf{X_{uu}}$, $\mathbf{Y_{vv}}$, and $\mathbf{Z_{ww}}$ (in lookup tables) as

$$\begin{bmatrix} X_D \\ Y_D \\ Z_D \end{bmatrix} = \begin{bmatrix} \mathbf{X_{uu}}|u|u \\ \mathbf{Y_{vv}}|v|v \\ \mathbf{Z_{ww}}|w|w \end{bmatrix}. \tag{23}$$

To include cross couplings, the hydrodynamic moments are modeled as a cross product of the hydrodynamic forces and a moment arm given by the position of the center of effort, $\mathbf{r_{cp}} = [\,\mathbf{x_{cp}}\ \mathbf{y_{cp}}\ \mathbf{z_{cp}}\,]^T$. The moment arm $\mathbf{r_{cp}}$ is also modeled as a function of the angle of attack and Reynolds' number within a lookup table. Additionally, hydrodynamic derivatives K_{pp}, M_{qq}, N_{rr} are included as rotational damping constants. The hydrodynamic moments $[\,K_D\ M_D\ N_D\,]^T$ are

$$\begin{bmatrix} K_D \\ M_D \\ N_D \end{bmatrix} = \begin{bmatrix} K_{pp}|p|p \\ M_{qq}|q|q \\ N_{rr}|r|r \end{bmatrix} + \mathbf{r_{cp}} \times \begin{bmatrix} X_D \\ Y_D \\ Z_D \end{bmatrix}. \tag{24}$$

Combining the hydrodynamic forces and moment calculations, the full nonlinear damping matrix $\boldsymbol{D}(\boldsymbol{\nu}) \in \mathbb{R}^{6\times 6}$ in (5) is assembled as (25), shown at the bottom of the page.

Lookup tables for $\mathbf{X_{uu}}$, $\mathbf{Y_{vv}}$, $\mathbf{Z_{ww}}$, and $\mathbf{r_{cp}}$ in the damping matrix $\boldsymbol{D}(\boldsymbol{\nu})$ are generated for the main hull body and the thrust vectoring nozzle (as a combination of NACA0015 airfoil profiles). The nonlinear damping coefficients and the moment arms are obtained by transforming the nondimensional flow coefficients C_L, C_D, and C_M to body fixed coordinates.

The upper right quadrant of the damping matrix in (25) is set as 0 because the cross coupling between the forces and angular velocities was seen to have a negligible effect for a slender AUV, as opposed to the significant cross coupling between moments and linear velocities. If included, the matrix would take the form, shown in (26), at the bottom of the next page, where the coefficients in the matrix represent hydrodynamic derivatives.

TABLE II
VERIFICATION, REMUS ($\mathrm{Re} = 2.9 \times 10^6$)

Coefficient(kg/m)	*From [9]*	*Jorgensen*	*DATCOM*
$\lvert X_{uu}\rvert_{(\alpha=0^\circ)}$	1.62	2.006	2.117
$\lvert Y_{vv}\rvert_{(\alpha=90^\circ)}$	1.31×10^2	0.643×10^2	0.554×10^2
$\lvert Z_{ww}\rvert_{(\alpha=90^\circ)}$	1.31×10^2	0.643×10^2	0.554×10^2

TABLE III
VERIFICATION, AUTOSUB AT 1 m/s ($\mathrm{Re} = 4.6 \times 10^6$)

Coefficient	*From [33]*	*Jorgensen*	*DATCOM*
$C_{D(\alpha=0^\circ)}$	9.7×10^{-3}	3.7×10^{-3}	8.6×10^{-3}

B. Multifidelity Hydrodynamic Database

1) Validation of Body Hydrodynamics: First, comparison is performed with known data from the literature on existing AUVs to verify the validity of the analytical and semiempirical methods used. Considering the REMUS AUV at $u = 1.5$ m/s, it can be seen in Table II that the values of X_{uu}, Y_{vv}, and Z_{ww} calculated for the REMUS hull at 0° angle of attack are similar to the predictions in [9], although the cross-flow terms are comparatively lower (it is to be noted that the predictions in [9] were later scaled and corrected for experimental conditions). Additionally, CFD computations of the drag coefficient C_D of the Autosub AUV from the National Oceanography Center are available in [32], and the C_D value at 1 m/s is also compared with predictions from Jorgensen's method and DATCOM (see Table III). Good

$$\boldsymbol{D}(\boldsymbol{\nu}) = \begin{bmatrix} \mathbf{X_{uu}}|u| & 0 & 0 & 0 & 0 & 0 \\ 0 & \mathbf{Y_{vv}}|v| & 0 & 0 & 0 & 0 \\ 0 & 0 & \mathbf{Z_{ww}}|w| & 0 & 0 & 0 \\ 0 & -\mathbf{z_{cp}}\mathbf{Y_{vv}}|v| & \mathbf{y_{cp}}\mathbf{Z_{ww}}|w| & K_{pp}|p| & 0 & 0 \\ \mathbf{z_{cp}}\mathbf{X_{uu}}|u| & 0 & -\mathbf{x_{cp}}\mathbf{Z_{ww}}|w| & 0 & M_{qq}|q| & 0 \\ -\mathbf{y_{cp}}\mathbf{X_{uu}}|u| & \mathbf{x_{cp}}\mathbf{Y_{vv}}|v| & 0 & 0 & 0 & N_{rr}|r| \end{bmatrix} \tag{25}$$

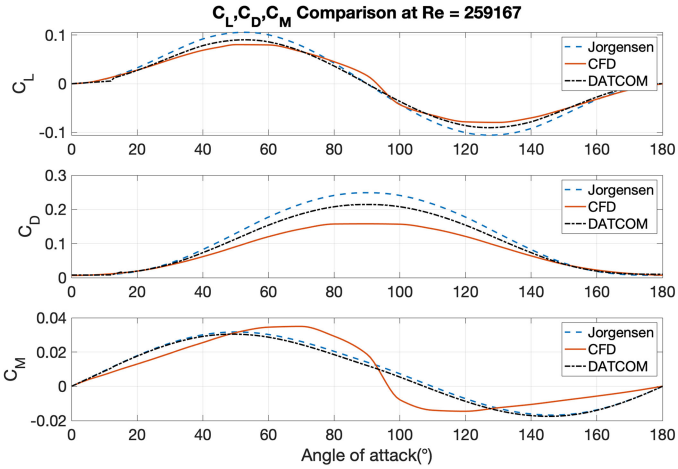

Fig. 9. Cross validation of body calculation methods: Jorgensen, DATCOM, and CFD at Re $= 2.6 \times 10^5$.

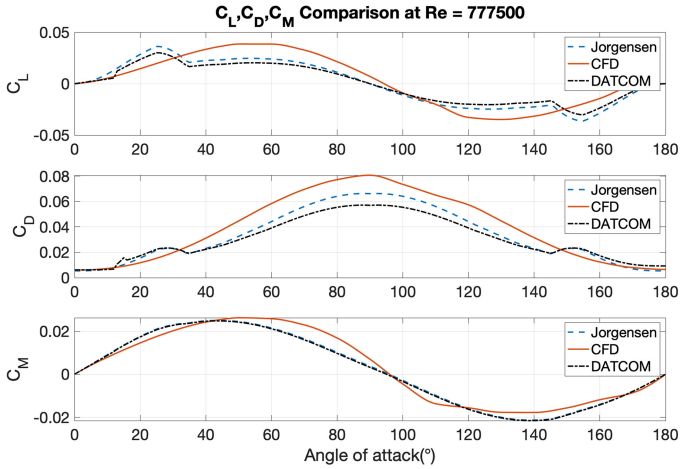

Fig. 10. Cross validation of body calculation methods: Jorgensen, DATCOM, and CFD at Re $= 7.8 \times 10^5$.

agreement is seen here with DATCOM, although the prediction diverges from [32] at higher Reynolds' numbers (Re$> 5 \times 10^6$).

Considering higher fidelity methods to validate body hydrodynamics, a Reynolds Averaged Navier-Stokes (RANS)-based CFD solver in Fluent is used to compute the flow around the body at selected Reynolds' numbers (the detailed study can be found in [19]). This provides high-fidelity snapshots of the flow at critical regions to improve accuracy. Focusing on SAM, the results from the different calculation methods in Section III are cross validated for all angles of attack at selected Reynolds' numbers where CFD simulations are performed. Existing studies such as [11] use Jorgensen's method for the full envelope hydrodynamics; so, this can be a basis for comparison in cross validation.

In Fig. 9 showing results at Re $= 2.6 \times 10^5$, it can be seen that predictions by DATCOM and Jorgensen's method match well with CFD results for the lift coefficient C_L. There is a divergence (up to a maximum of 40% between Jorgensen and CFD) when approaching 90° angle of attack between the three methods for the drag coefficient C_D. In the case of the pitching moment coefficient C_M, DATCOM and Jorgensen's method offer similar predictions, whereas the CFD result shows divergence (up to 70%) and hysteresis at high angles of attack close to 90°.

In Fig. 10, at Re $= 7.8 \times 10^5$, it can be seen that the predictions follow a similar pattern as before, but there is a drop in magnitude by a factor of 10. A clear transition region is seen at around 35° and 145° angles of attack for the DATCOM and Jorgensen curves. It is also seen that the prediction of C_D matches

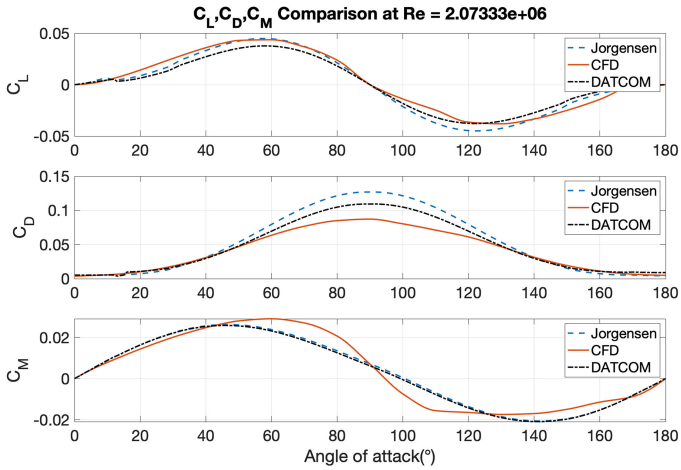

Fig. 11. Cross validation of body calculation methods: Jorgensen, DATCOM, and CFD at Re $= 2.1 \times 10^6$.

better with CFD results. In Fig. 11, analytical and semiempirical predictions match quite closely with CFD results for C_L and C_M (although divergence between methods of the order of 50% is seen close to 90°). The behavior for C_D prediction is similar to the previous cases.

From these comparisons, it can be seen that DATCOM can be a good base calculation that offers reasonable agreement with CFD results (with the maximum deviation at regions close to 90°). In transition regions for C_D, Jorgensen's method offers a closer prediction to CFD results. DATCOM can be seen as an augmentation of Jorgensen's method at low angles of attack.

$$\boldsymbol{D}(\boldsymbol{\nu}) = \begin{bmatrix} X_{uu}|u| & 0 & 0 & 0 & X_{qq}|q| & -X_{rr}|r| \\ 0 & Y_{vv}|v| & 0 & -Y_{pp}|p| & 0 & Y_{rr}|r| \\ 0 & 0 & Z_{ww}|w| & Z_{pp}|p| & -Z_{qq}|q| & 0 \\ 0 & -K_{vv}|v| & K_{ww}|w| & K_{pp}|p| & 0 & 0 \\ M_{uu}|u| & 0 & -M_{ww}|w| & 0 & M_{qq}|q| & 0 \\ -N_{uu}|u| & N_{vv}|v| & 0 & 0 & 0 & N_{rr}|r| \end{bmatrix} \tag{26}$$

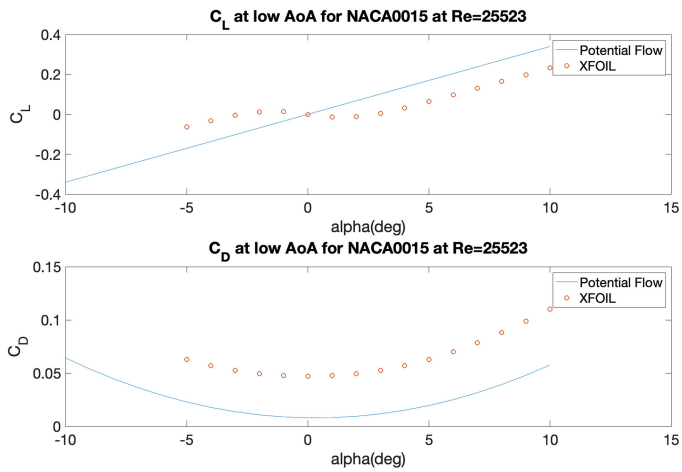

Fig. 12. Cross validation of control surface calculation methods: Lifting line (solid line) and XFOIL (circles) at Re $= 2.6 \times 10^4$.

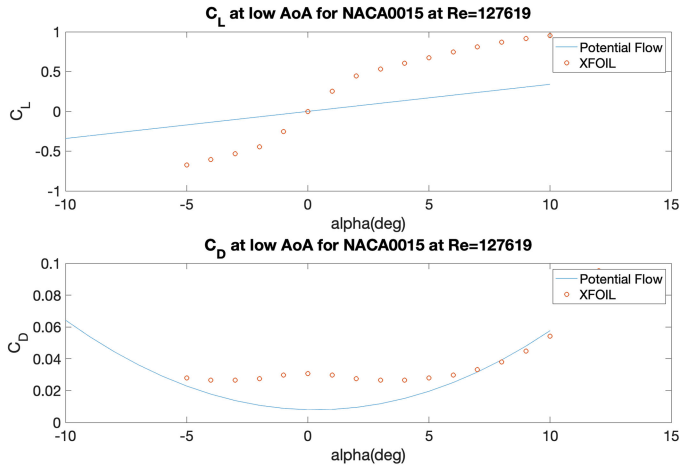

Fig. 13. Cross validation of control surface calculation methods: Lifting line (solid line) and XFOIL (circles) at Re $= 1.3 \times 10^5$.

2) Validation of Wing Hydrodynamics: Cross validation of control surfaces at low angles of attack is performed using XFOIL at angles of attack between -5° and 12°. In Fig. 12, at Re $= 2.6 \times 10^4$, it can be seen that lifting line prediction matches well for C_L, but there is a constant offset in the case of C_D. In Fig. 13, at Re $= 1.3 \times 10^5$, the lifting line result for C_L underpredicts the value compared to the XFOIL result, but the result for C_D matches quite well.

3) Hydrodynamic Database Synthesis: Following cross verification, database synthesis for the SAM body is performed using Algorithm 1 over a range of Reynolds' numbers corresponding to velocities between 0.1 and 5 m/s, over the full -180° to 180° angle-of-attack envelope. As listed in Table IV, interpolated CFD results are prioritized at low angles of attack within the Reynolds' number range considered. At higher angles of attack, Jorgensen's method is selected. For Reynolds' numbers outside the range of the CFD analysis, DATCOM is used over the full envelope. The results can be seen in Figs. 14 –16. There is a jump on switching between different methods, especially while switching to DATCOM at high Reynolds' numbers (see Fig. 16).

TABLE IV
SUMMARY OF METHODS USED FOR THE SAM DATABASE

Components	Re	α	*Methods*
Body	$\leq 3.9 \times 10^6$	$0 - 20^\circ$	CFD (interpolated with *makima*)
		$20 - 180^\circ$	Jorgensen's method
	$> 3.9 \times 10^6$	$0 - 180^\circ$	DATCOM
Control surfaces	all	$0 - 10^\circ$	Lifting line theory
		$10 - 180^\circ$	Flat plate theory

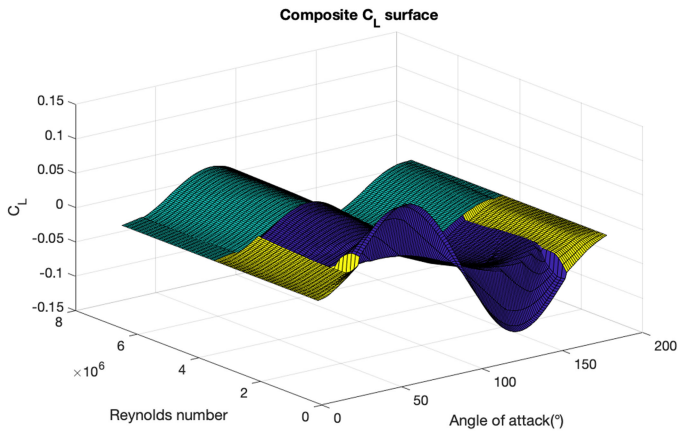

Fig. 14. Synthesized body lift coefficient C_L (Legend: Yellow—CFD, blue—Jorgensen, cyan—DATCOM).

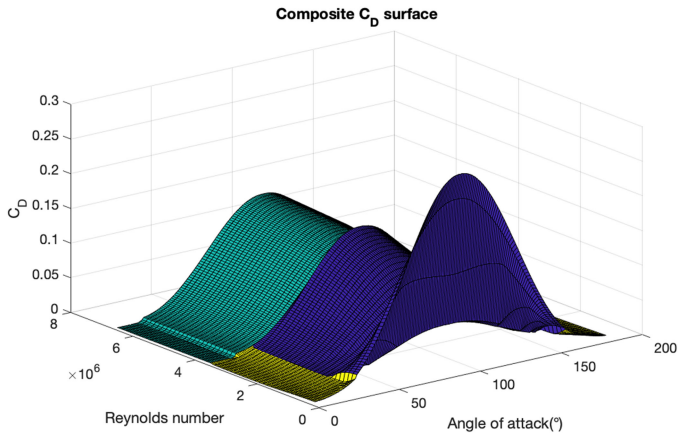

Fig. 15. Synthesized body drag coefficient C_D (Legend: Yellow—CFD, blue—Jorgensen, cyan—DATCOM).

The hydrodynamic database for the control surfaces comprising the SAM thrust vectoring nozzle is similarly synthesized using Algorithm 2 and smoothed using Montgomerie's method, generating the surfaces presented in Fig. 17.

The calculation methods used and the range for the body and the control surfaces in the thrust vectoring nozzle are summarized in Table IV. Example data sets for the SAM hull body and an NACA0015 airfoil are provided in the supplementary material, and can be viewed by running the script *Datasets.m*.

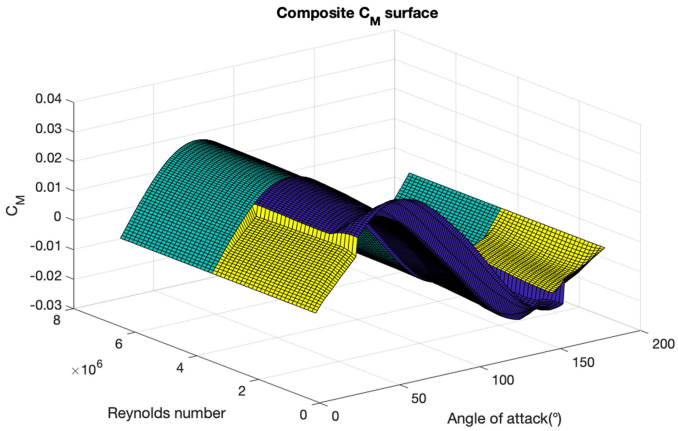

Fig. 16. Synthesized body pitching moment coefficient C_M (Legend: Yellow—CFD, blue—Jorgensen, cyan—DATCOM).

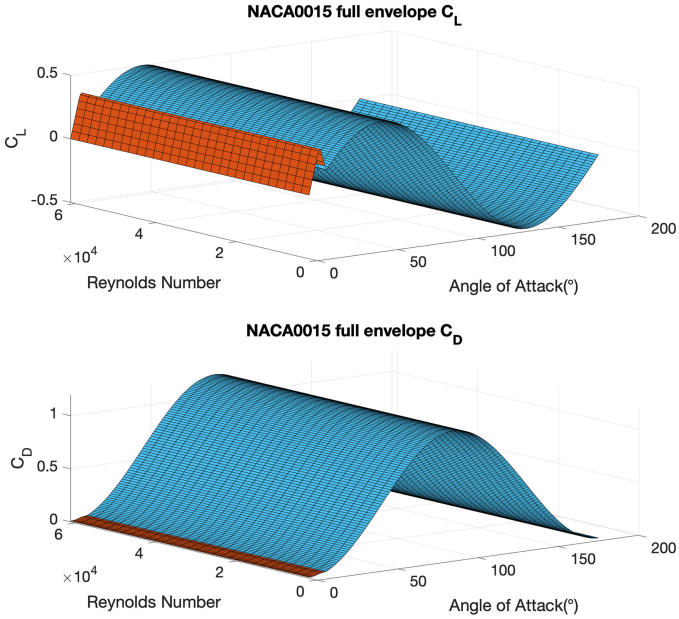

Fig. 17. Synthesized drag and lift coefficients for an NACA0015 airfoil profile over the $0^\circ - 180^\circ$ angle-of-attack envelope (Legend: Red—lifting line, blue—flat plate).

C. Simulations of Hydrobatic Maneuvers

First, a performance check is done on the simulation model by monitoring simulation parameters over an accelerating horizontal turn up to 90° yaw angle. The idea is to push the simulation model over an extended range of Reynolds' numbers and angles of attack. The AUV is accelerated from 0 to 5 m/s by steadily increasing the propeller revolutions per minute, with the horizontal thrust vectoring (rudder) angle set to a maximum deflection of 7°. Three full envelope hydrodynamic data sets are evaluated—Jorgensen's method (as used in [11]), interpolated CFD results (as presented in [19]), as well as the presented multifidelity database. The simulations are run on a standard laptop (Macbook Pro 2017). A solver profiler tool in Simulink[3] is used to monitor simulator parameters including the *simulation time/real time ratio* (a value less than 1 means that the simulation is faster than real time), the solver time step, number of zero crossings per 100 s (this means the solver is reset to improve accuracy), and the CPU usage of subroutines.

[3]Online. [Available]: https://se.mathworks.com/help/simulink/slref/solverprofiler.html

TABLE V
MONITORED SIMULATOR PERFORMANCE FOR AN ACCELERATING TURN

Parameter	*Value*
Simulation Time / Real Time Ratio	1.2
Solver Used	Matlab ODE45 (Runge Kutta)
Solver Time Step	Variable (Min: 10^{-5}s, Max: 1s)
Zero crossings per 100s	45
Functions with high CPU Usage	Solver and Integrator Damping interpolation Hydrostatics Trim subsystems Plotting

These performance parameters are recorded in Table V. In comparing the data sets, all three data sets had a similar simulation-time/real-time ratio of 1.2, with a maximum deviation of 14% in recorded positions and orientations, and 20% in linear and angular velocities. Interpolating the hydrodynamic forces from the lookup tables consumes the most processing time (with the hull requiring significantly more effort than the control surfaces). The simulation is faster than real-time for simple maneuvers (with the ratio going as low as 0.4), and it can go up to more than twice as long as real-time for complex hydrobatic maneuvers with significant nonlinear effects (since very small time steps are needed in critical sections). Real-time and close-to-real-time simulations are, therefore, possible.

The multifidelity data set is used for subsequent hydrobatics simulations in this case study. The objectives of these simulations are to demonstrate hydrobatic maneuvering capabilities and validate the simulation method at full envelope maneuvers.

1) Tight Looping Maneuver: A tight looping maneuver can be achieved by using a so-called turbo-turn sequence on the thrust vector system. This means that the propellers and vertical thrust vector are cycled asynchronously between maximum positive and negative values (see Fig. 18) so that the surge-direction thrust is essentially canceled out and a maximum turning thrust is achieved (consequently the name turbo-turn). The AUV can, thereby, perform a turning maneuver with a very small turning radius. Here, this is visualized in Fig. 19 in the vertical plane, and it can be seen that the AUV remains in a box of dimension of 5 m. In Fig. 20, it can be seen that the pitch angle goes up to 180°, meaning that the AUV undergoes a flip.

2) Tight Horizontal Turning: This maneuver is used to make the AUV perform very tight turns horizontally in a confined area (see Fig. 21), by using the turbo-turn strategy, together with the

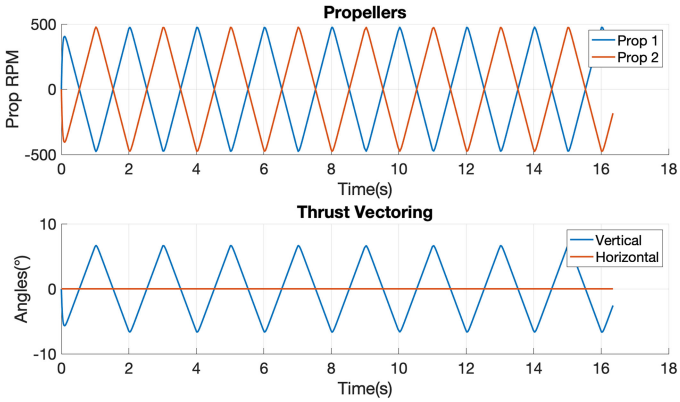

Fig. 18. Snapshot of actuator commands for tight looping maneuver.

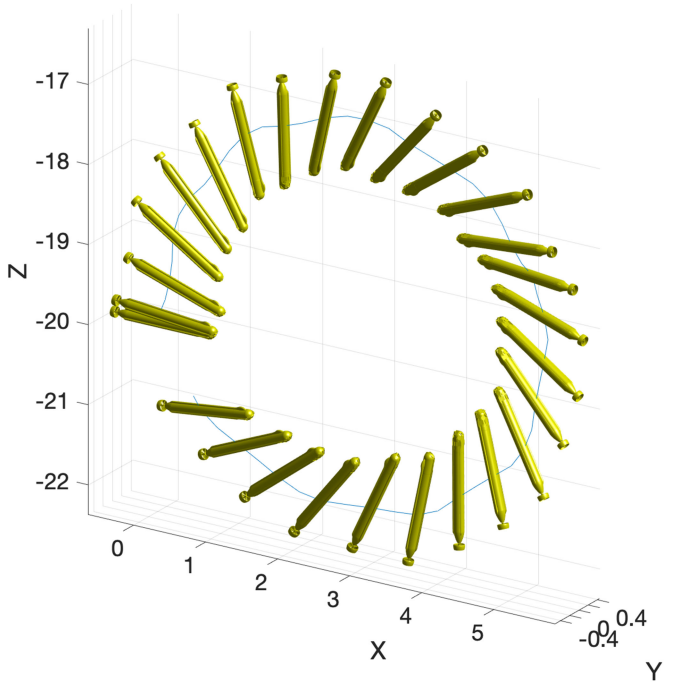

Fig. 19. Trajectory of tight looping maneuver (unit: meter).

trim subsystems stabilizing the AUV (see Fig. 22). This enables a horizontal sweep in the yaw direction (see Fig. 23).

3) Helix Maneuver: Building on the turbo-turn maneuver above considering both pitch and yaw degrees of freedom, a helix maneuver can be achieved, enabling a helical inspection in a confined area. The horizontal thrust vector is also used, and actuator commands are as presented in Fig. 24. From the AUV trajectory (in Fig. 25) and states (see Fig. 26), it is clear that the AUV model can perform an agile maneuver considering high angles of attack and side slip in a confined box, thus opening the door to interesting new inspection strategies.

4) Stationary LCG Sweep Maneuver: In addition, the trim subsystems may be employed as an additional option to maximize maneuvering capacity and minimize the use of the thrusters (e.g., for inspection of objects near sediment layers). The LCG trim subsystem can, thus, be utilized to enable a vertical sweep using only the trim subsystems. With the AUV level (with neutral

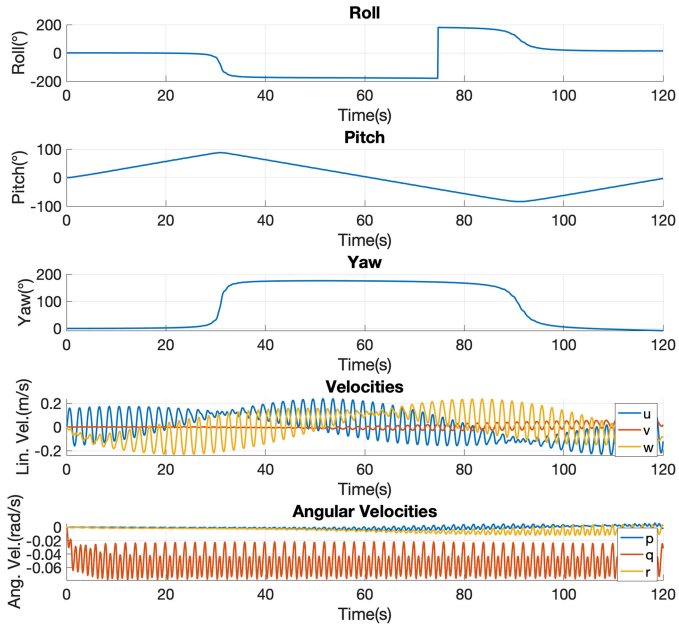

Fig. 20. Angles and velocities of tight looping maneuver. The pitch goes through the full envelope.

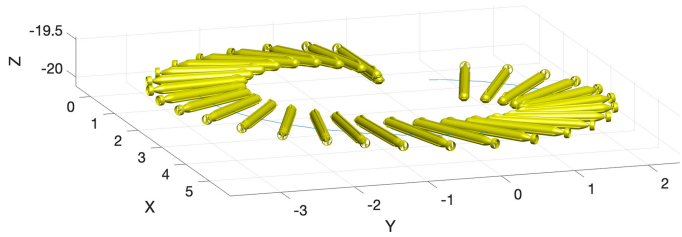

Fig. 21. Trajectory of turbo-turn maneuver (unit: meter).

buoyancy thanks to the VBS) without the propeller activated, the LCG (and, thus, the c.g. position) is set all the way forward, causing the AUV to pitch downwards, and then set all the way back, causing the AUV to pitch upward (see Fig. 27). From the AUVs trajectory (see Fig. 28) and states (see Fig. 29), it can be seen that the AUV model is very agile in pitch, with just the use of the LCG subsystem.

D. Experimental Validation in Field Tests

The simulations are qualitatively compared to the results of real-world tests of hydrobatic maneuvering performed with the SAM AUV. The motivation of the tests was to further validate the simulation model, and to evaluate the applicability of the simulator as a development tool. The turbo-turn maneuver has been evaluated with the SAM AUV in a field test in Kristineberg on the Swedish west coast. During the field test, pitch and depth control was performed with PID controllers using the LCG and VBS subsystems, making sure the AUV was submerged at a depth of 0.5 m (see [2] for more information on the control systems). The counterrotating propellers were both set at ± 1000 r/min, and the effective rudder angle commanded to the thrust vectoring system was set to $\pm 5^{\circ}$, with an input sequence similar to Fig. 22. The

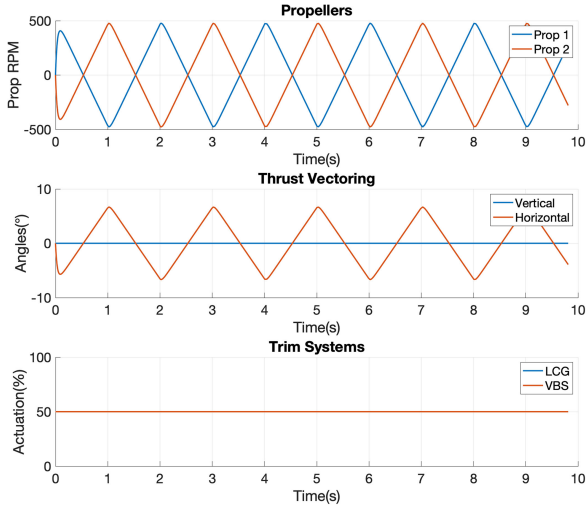

Fig. 22. Snapshot of actuator commands for turbo-turn maneuver.

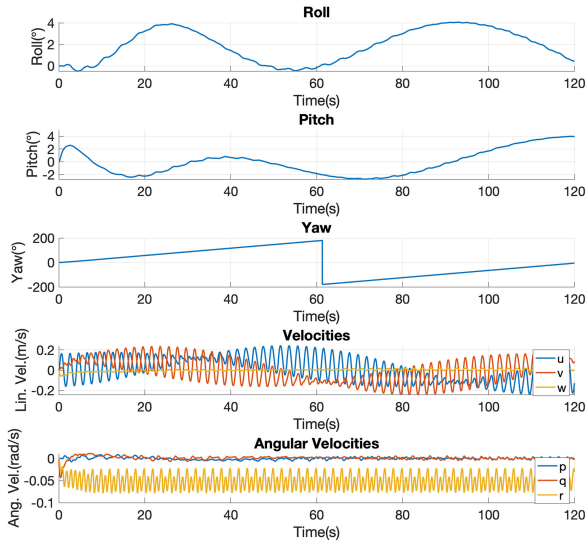

Fig. 23. Angles and velocities of turbo-turn maneuver. The yaw encompasses the full envelope.

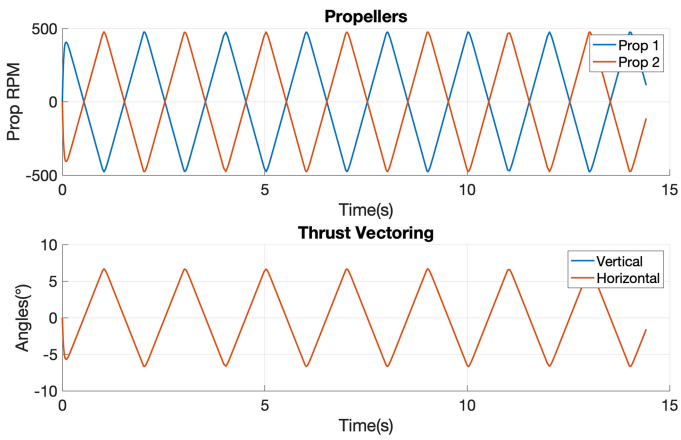

Fig. 24. Snapshot of actuator commands for helix maneuver.

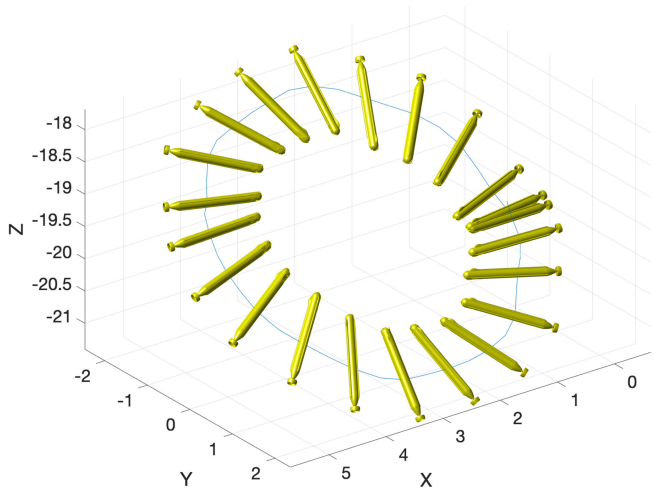

Fig. 25. Trajectory of helix maneuver (unit: meter).

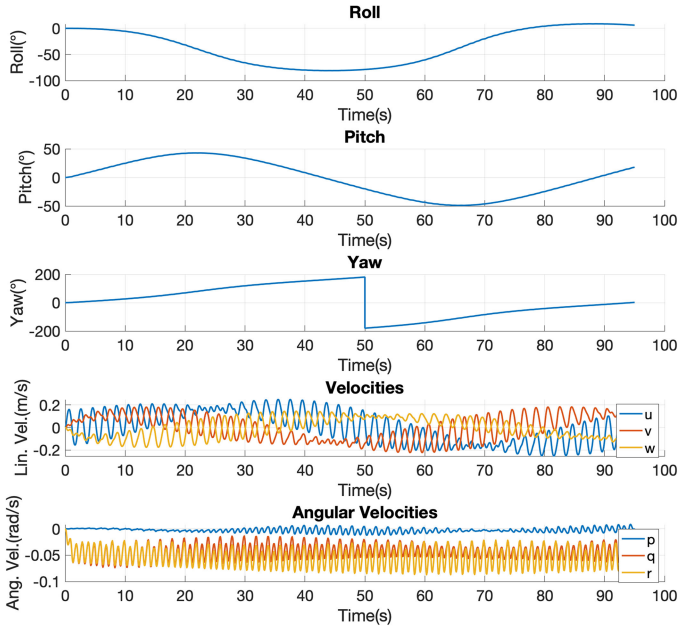

Fig. 26. Angles and velocities of helix maneuver. The roll and yaw encompass the full envelope.

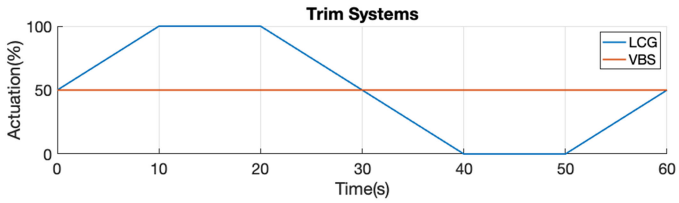

Fig. 27. Actuator commands for LCG sweep maneuver.

AUV was made to perform a turbo-turn over 90° yaw angle. The scenario is replicated in the hydrobatics simulator with the same input sequence and initial vehicle state (with the VBS and LCG positions constant at 50%).

The behavior of the simulation model is qualitatively similar to the real vehicle during the maneuver. Comparing sensor

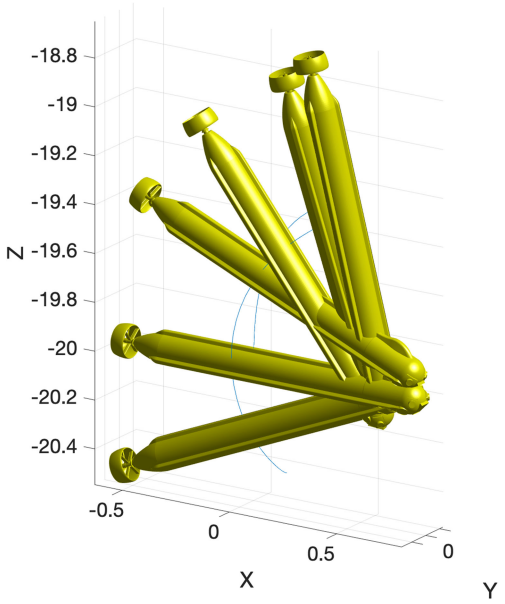

Fig. 28. Trajectory of LCG sweep maneuver (unit: meter). The maneuver enables static pitch control.

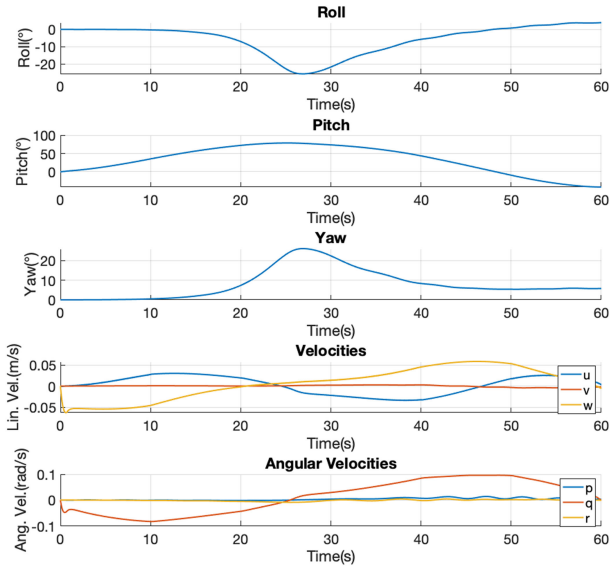

Fig. 29. Angles and velocities of LCG sweep maneuver. Note that the pitch angle reaches almost 90°.

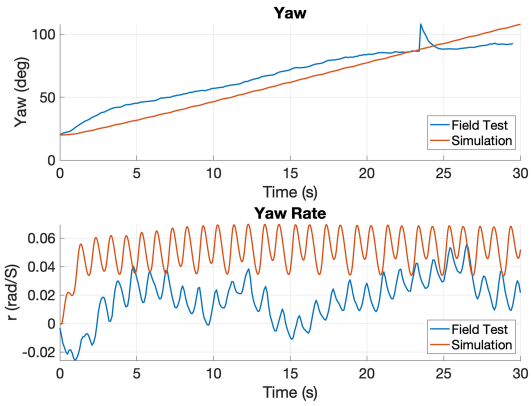

Fig. 30. Comparison of yaw angle and rate for a turbo-turn maneuver between a simulation run (red) and field test (blue). The data from the field test and simulation for the yaw angle and yaw rate are available in the supplementary material.

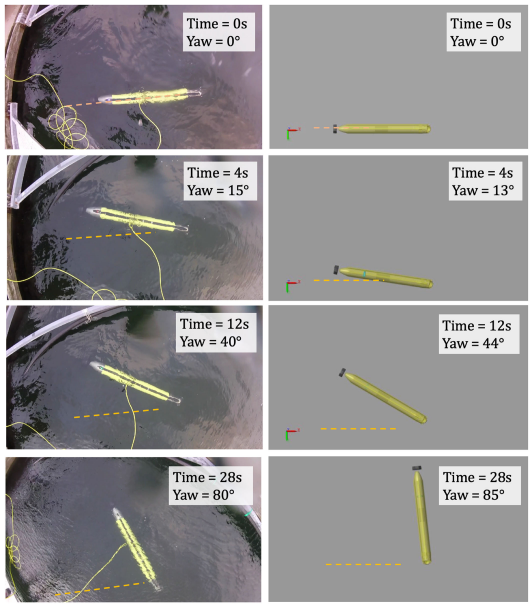

Fig. 31. Behavior of the AUV in field tests during the turbo-turn maneuver in a field experiment (left) is qualitatively similar to the simulated motion (right). This enables the use of the simulator as a development tool, as maneuvers and control strategies can be pretested in simulation. Full video footage of the real and simulated maneuvers side by side is available in the supplementary material in Video 1.

feedback on SAM with the simulation in Fig. 30, it can be seen that the yaw angle of the AUV is similar in both simulation and experiment. There is an instantaneous jump in the yaw angle at $t = 24$ s, which was due to an occasional jump in IMU output. The yaw rate follows a similar trend, with the same oscillation frequency close to 1 Hz. There is a second harmonic in the experimental yaw rate plot, and this can be attributed to cross-couplings, external disturbances, as well as actions by internal subsystems to compensate for the same. For example, moving the thrust vectoring system affects the vehicle's center-of-gravity position, which in turn induces a rolling moment. Additionally, the propellers influence the pitch angle as well as the roll. The LCG and VBS subsystems compensated for these disturbances in the field test. Furthermore, the tests were performed close to a dock with currents, so these currents could also have had an influence.

Videos from the simulation and the experiment can be observed side by side in Video 1 in the supplementary material. Snapshots of the top view of a right hand turbo-turn are presented in Fig. 31. To further support the sensor data, it can be seen that the simulation shows good agreement with real-world behavior, and the motion of the real AUV matches closely with the simulation model. This motivates the use of the simulator as a development tool to test aggressive hydrobatic maneuvers at low risk. In addition to the turbo-turn maneuver, simulations of the tight looping and helix maneuvers are also available in the supplementary material in Video 1.

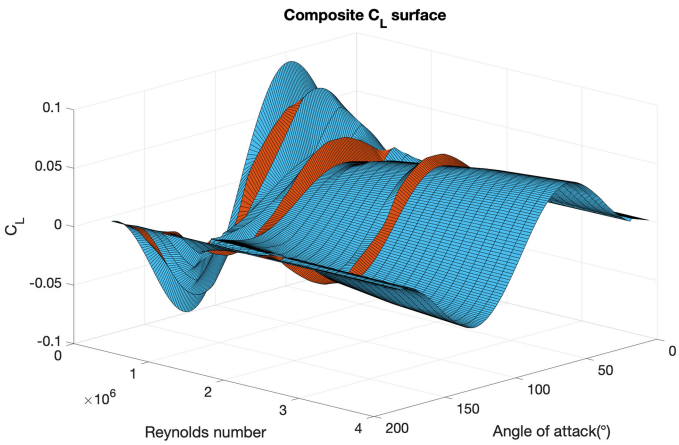

Fig. 32. Discontinuities are caused in the multifidelity database [e.g., between CFD (red) and DATCOM (blue)] if discrete datapoints are used without smoothing. This can lead to unrealistic jumps/ nonlinearities in simulation.

VI. Discussion

A. Multifidelity Hydrodynamic Database

The generalized method described in this article offers a relatively easy and straightforward solution to synthesize a hydrodynamic model over the full envelope. This article presents validation with existing literature, cross validation between methods and maneuvering simulations. With a realistic set of coefficients, it is shown that the simulator can offer good performance. The accuracy of the hydrodynamic database depends on the flow scenario, as well as on the methods used to generate the data sets. The suggested multifidelity database can be populated with data from different flow scenarios and based on different methods. Some examples are provided in the case study but there can be many other ways of adding data, which then depends on operational scenarios (e.g., shape of vehicle, flow conditions, range of Reynolds numbers, etc.). The accuracy of the simulations depends on these data sets and can, thus, vary largely between different users. While this case study focuses on slender torpedo-shaped vehicles, a similar approach can be used to build up data sets for other shapes, using the best available data from analytical calculations, CFD simulations, and experiments. Added mass effects may need to be considered for aggressive and fast maneuvers with a similar lookup table approach (e.g., [33]). Similitude can be used to scale the results to different vehicle dimensions and flow velocities, but care must be taken to consider if interactions and coupling effects are significant (e.g., for small micro-AUVs).

Regions of transition between flow regimes or data sets can create unrealistic discontinuities or additional nonlinearities in the dynamic model (see Fig. 32), and smoothing these discontinuities is a key challenge in creating robust full-envelope simulations. Therefore, the database buildup algorithm, and the selection of appropriate data sets, were crucial in enabling realistic simulations. If very accurate flow snapshots are available at particular points, appropriate interpolation is necessary to avoid discontinuities, as seen in Fig. 32. The simulation time is affected by the time it takes to interpolate between data-points within the hydrodynamic data set. Thus, the presence of discontinuities in the data sets can lead to slower simulations, since a smaller solver time step is needed for effective interpolation. While these discontinuities do not affect simple maneuvers, they can cause issues in simulating dynamic and aggressive maneuvers such as the turbo-turn.

A valuable improvement in future work would be on the prediction methods used in the hydrodynamic database with regards to interaction effects between components, and flow memory or hysteresis effects. These could be a cause of large inaccuracies as well as unexpected behaviors. Here, system identification methods to identify models for these effects from field experiments can be a very interesting track to pursue.

B. Flight Simulations, Validation, and Application

The ability to simulate advanced maneuvers in close to real time on a standard PC offers a powerful development tool in the design of controller policies. It is feasible and valuable to prototype new hydrobatic maneuvers within the simulator, and this offers a crucial piece of a cyber-physical system for virtual validation [2]. It is seen that the simulation model matches reasonably well with field measurements for the turbo-turn maneuver. However, a key challenge for further validation is the availability of a precise sensor suite to obtain a valid ground truth, especially for underwater positioning. The use of bathymetric SLAM, visual odometry, motion capture cameras, or acoustic localization would be of benefit in enabling further verification and validation. Validation of full envelope simulation results with field experiments has been a challenge in past work such [11] as well here a steady circular turn maneuver was used for checking the turning radius.

Interoperability, and modeling whole scenarios and external disturbances, can add significant value to the simulator as a development tool. Studies have already been performed on controller design using this simulator, which is the scope of further research. Also of interest is the possibility of extracting a simplified hydrodynamic model for use in model predictive controller design. An interesting point for future work is to translate the multifidelity method presented here to open-source robotics simulation environments such as Stonefish [34]. This can enable the use of higher fidelity flight dynamics models to enable virtual validation of autonomy software for maneuvers, tasks as well as full missions.

C. Simulator Performance Against Requirements

Revisiting the simulator requirements in terms of accuracy, efficiency, and applicability, real-time or close to real-time flight simulations can be performed using the generalized framework, and the maneuvers studied have included the full flight envelope. Simulations performed with different data sets (Jorgensen, CFD or the multifidelity database) can show deviations in positions and velocities, depending on the flow scenario (in terms of angle of attack and Reynolds number). There is, thus, a potential to augment the models presented in existing literature that use only Jorgensen's method (such as [11]), using the multifidelity lookup tables. For example, if good quality CFD results are

available at low angles of attack, these can be used to augment the existing Jorgensen data sets. The ability to combine different data sets effectively is a key to balance accuracy and efficiency.

The use of multifidelity lookup tables balances the potential accuracy gain from numerical methods such as CFD with the efficiency gain of analytical semiempirical methods. Performing a series of CFD calculations such as in [19] to compute the hydrodynamic coefficients over the full envelope can take between 3 h and a few days depending on the angular resolution and solver convergence (further information on the time taken for CFD studies can be found in [21]). Thus, using CFD simulations alone can be prohibitively expensive for designing controllers, and may not be a useful engineering tool for that purpose (especially due to the lack of real-time solutions). However, this article shows that the presented multifidelity approach can achieve reasonable accuracy with close to real-time simulation speeds offering a powerful engineering tool for controller design of advanced maneuvers.

The requirements of efficiency and applicability are shown, while the accuracy is quantifiable for most use cases with a known pathway for improvement (since the accuracy is linked to the quality of the data set used). The workflow presented and the simulation framework is flexible and scalable, enabling relatively easy updates, extensions, and modifications.

VII. Conclusion

This article presents a strategy for assembling a multifidelity database in the modeling of advanced hydrobatic maneuvers for underwater vehicles. Such a strategy enables real-time simulation over the full flight envelope.

A number of different methods for populating such multifidelity database are presented and evaluated. Comparisons are made to data from existing literature as well as to data generated from CFD simulations. An example simulator framework is also presented based on the proposed approach and simulations of advanced maneuvers are performed and compared to experimental field trials.

To conclude, the strategy presented offers a simple and relatively straightforward way of simulating advanced maneuvers in real time (or close to real time). This enables direct use of the simulations as efficient tools in controller design. Simulations correlate qualitatively well with the experimental results, and simulated maneuvers are shown to behave reasonably close to real-world results. This can, therefore, minimize the need for large-scale tuning of controllers once implemented on real vehicles. Furthermore, this framework also provides a useful tool in future research on reinforcement learning and system identification strategies to achieve even more accurate dynamics models and controller designs.

Some of the key open challenges include discontinuities between methods, hysteresis effects, and interaction effects. System identification from experimental data is also a possible means for expanding on the database and the dynamics model for higher accuracy.

Acknowledgment

The authors would like to thank Josefine Severholt for providing the 3-D CAD model of the SAM AUV for plots and simulations.

References

[1] S. Bhat and I. Stenius, "Hydrobatics: A review of trends, challenges and opportunities for efficient and agile underactuated AUVs," in *Proc. IEEE/OES Auton. Underwater Veh. Workshop*, Nov. 2018, pp. 1–8.

[2] S. Bhat, I. Stenius, N. Bore, J. Severholt, C. Ljung, and I. T. Balmori, "Towards a cyber-physical system for hydrobatic AUVs," in *Proc. OCEANS Conf.*, Marseille, France Jun. 2019, pp. 1–7.

[3] S. Bhat *et al.*, "A cyber-physical system for hydrobatic AUVs: System integration and field demonstration," in *Proc. IEEE/OES Auton. Underwater Veh. Symp.*, Sep. 2020, pp. 1–8.

[4] T. Fossen, *Handbook of Marine Craft Hydrodynamics and Motion Control*. Hoboken, NJ, USA: Wiley, Apr. 2011.

[5] A. J. Healey and D. Lienard, "Multivariable sliding mode control for autonomous diving and steering of unmanned underwater vehicles," *IEEE J. Ocean. Eng.*, vol. 18, no. 3, pp. 327–339, Jul. 1993.

[6] J. Silva and J. Sousa, "Models for simulation and control of underwater vehicles," in *New Approaches in Automation and Robotics*, H. Aschemann, Ed. Rijeka, Croatia: IntechOpen, 2008, ch. 11.

[7] D. P. Brutzman, "A virtual world for an autonomous underwater vehicle," Ph.D. dissertation, Dept. Comput. Sci., Naval Postgraduate Schl. Monterey, CA, USA, 1994.

[8] M. Nahon, "A simplified dynamics model for autonomous underwater vehicles," in *Proc. Symp. Auton. Underwater Veh. Technol.*, 1996, pp. 373–379.

[9] T. Prestero, "Verification of a six-degree of freedom simulation model for the REMUS autonomous underwater vehicle," Ph.D. dissertation, Massachusetts Inst. Technol., Department of Ocean Engineering, Cambridge, MA, USA, 2011.

[10] K. P. Watson, J. S. Webster, J. W. Crane, and N. S. Smith, "Prediction of submersible maneuvering performance at high incidence angles," in *Proc. OCEANS Conf.*, Oct. 1993, vol. 2, pp. II289–II294.

[11] J. Evans and M. Nahon, "Dynamics modeling and performance evaluation of an autonomous underwater vehicle," *Ocean Eng.*, vol. 31, pp. 1835–1858, Oct. 2004.

[12] L. H. Jorgensen, "Prediction of static aerodynamic characteristics for space-shuttle-like and other bodies at angles of attack from 0 deg to 180 deg," Nat. Aeronaut. Space Admin., Washington, DC, USA, Tech. Rep. 19730006261, 1973.

[13] V. Dyke, Ed., *An Album of Fluid Motion*, 4th ed. Stanford, CA, USA: Parabolic Press, 1982.

[14] R. M. Cummings, J. R. Forsythe, S. A. Morton, and K. D. Squires, "Computational challenges in high angle of attack flow prediction," *Prog. Aerosp. Sci.*, vol. 39, no. 5, pp. 369–384, 2003.

[15] M. Selig, "Real-time flight simulation of highly maneuverable unmanned aerial vehicles," *J. Aircraft*, vol. 51, pp. 1705–1725, 2014.

[16] SNAME, *Nomenclature for Treating the Motion of a Submerged Body Through a Fluid (Tech. Res. Bull., no. 1–5)*. New York, NY, USA: SNAME, Apr. 1950.

[17] T. I. Fossen and A. Ross, "Nonlinear modelling, identification and control of UUVs," in *Guidance and Control of Unmanned Marine Vehicles (IEEE Control Eng. Ser.)*, G. Roberts and B. Sutton, Eds., 2006, ch. 2, pp. 23–42, doi: 10.1049/PBCE069E_ch2IET Digital Library, https://digital-library.theiet.org/content/books/10.1049/pbce069e_ch2

[18] R. D. Finck, "USAF (United States Air Force) stability and control DATCOM (Data Compendium)," McDonnell Aircraft Co., St. Louis, MO, USA, Tech. Database DTIC ADB072483, Apr. 1978.

[19] T. Miao, "Generation of a full-envelope hydrodynamic database for hydrobatic AUVs: Combining numerical, semi-empirical methods to calculate AUV hydrodynamic coefficients," Master's thesis, KTH Roy. Inst. Technol., Department of Aeronautical and Vehicle Engineering, Stockholm, Sweden, Aug. 2019.

[20] M. Drela, "XFOIL: An analysis and design system for low Reynolds number airfoils," in *Low Reynolds Number Aerodynamics*, T. J. Mueller, Ed. Berlin, Germany: Springer, 1989, pp. 1–12.

[21] A. B. Phillips, Simulations of a self propelled autonomous underwater vehicle," Ph.D. dissertation, School Eng. Sci., Univ. Southampton, Southampton, U.K., 2010.

[22] D. A. Jones, D. B. Clarke, I. B. Brayshaw, J. L. Barillon, and B. Anderson, "The calculation of hydrodynamic coefficients for underwater vehicles," Defence Sci. Technol. Org., Canberra, VIC, Australia, Tech. Rep., DSTO-TR-1329, Jul. 2002.
[23] M. T. Issac *et al.*, "Hydrodynamic analysis of AUV hulls using semi-empirical and CFD approach," *Universal J. Mech. Eng.*, vol. 5, no. 5, pp. 137–143, 2017.
[24] M. Nahon, "Determination of undersea vehicle hydrodynamic derivatives using the USAF Datcom," in *Proc. OCEANS Conf.*, vol. 2, Oct. 1993, pp. II283–II288.
[25] E. J. Hopkins, "A semi-empirical method for calculating the pitching moment of bodies of revolution at low Mach numbers," Nat. Advisory Committee Aeronaut., Boston, MA, USA, Tech. Rep. 19730006261, 1951.
[26] J. H. Ferziger and M. Peric, *Computational Methods for Fluid Dynamics*. Berlin, Germany: Springer, 2012.
[27] J. L. Petrilli, R. C. Paul, A. Gopalarathnam, and N. T. Frink, "A CFD database for airfoils and wings at post-stall angles of attack," in *Proc. 31st AIAA Appl. Aerodyn. Conf.*, 2013, Art. no. 2916.
[28] M. Tomac, "Towards automated CFD for engineering methods in aircraft design," Ph.D. dissertation, Dept. Aeronaut. Veh. Eng., KTH Roy. Inst. Technol., Stockholm, Sweden, 2014.
[29] E. Houghton and P. Carpenter, *Aerodynamics for Engineering Students*, 5th ed. Oxford, U.K.: Butterworth-Heinemann, 2003.
[30] B. Montgomerie, "Methods for root effects, tip effects and extending the angle of attack range to -180 °, with application to aerodynamics for blades on wind turbines and propellers," FOI Swedish Defence Res. Agency, Stockholm, Sweden, Tech. Rep. FOI-R-1305-SE, Jun. 2004.
[31] S. Bhat, I. Stenius, N. Bore, J. Severholt, C. Ljung, and I. T. Balmori, "Towards a cyber-physical system for hydrobatic AUVs," in *Proc. OCEANS Conf.*, Jun. 2019, pp. 1–7.
[32] A. Phillips, M. Furlong, and S. R. Turnock, "The use of computational fluid dynamics to assess the hull resistance of concept autonomous underwater vehicles," in *Proc. OCEANS Conf. Eur.*, Jun. 2007, pp. 1–6.
[33] J. Severholt, "Generic 6-DOF added mass formulation for arbitrary underwater vehicles based on existing semi-empirical methods," Master's thesis, Schl. Eng. Sci., KTH Roy. Inst. Technol., Stockholm, Sweden, 2017.
[34] P. Cieślak, "Stonefish: An advanced open-source simulation tool designed for marine robotics, with a ROS interface," in *Proc. OCEANS Conf.*, Marseille, France Jun. 2019, pp. 1–6.

Sriharsha Bhat (Member, IEEE) received the bachelor's degree in mechanical engineering from the National University of Singapore, Singapore, in 2013, and a master's degree in vehicle engineering in 2016 from the Royal Institute of Technology, Stockholm, Sweden, where he is currently working toward the Ph.D. degree in vehicle engineering focusing on the control and simulation of underwater robots.

From 2013 to 2014, he was a Research Engineer with the Singapore MIT Alliance for Research and Technology (SMART), Singapore, focusing on aerial and underwater robotics; and from 2016 to 2018, he was a Technology Development Engineer with Continental, Hannover, Germany. His research interests include optimal and model predictive control, motion planning, reinforcement learning, simulation/modeling, and system identification for robots and autonomous vehicles in challenging field applications.

Ivan Stenius (Member, IEEE) received the M.Sc. and Technical Licentiate degrees in lightweight structures in 2003 and 2007, respectively, from the Royal Institute of Technology (KTH), Stockholm, Sweden, and the Doctor in Technology degree in lightweight structures on hydroelasticity and fluid structure interactions on high-speed craft from KTH in 2009.

He is currently a full-time Associate Professor with the Department of Aeronautics and Vehicle Engineering, KTH. He has expertise in underwater vehicle modeling design and construction, as well as maneuvering and navigation. He has been the Lead Developer of Design and Analysis Software Tools in collaboration with FMV and The Swedish Coast Guard. He has been a PI for a number of research projects in collaboration with the Swedish Defence Material Administration, involving cross-disciplinary collaboration between the research groups—computer vision and perception, applied electrochemistry, and networked control at KTH. In the recent years, he has been heavily involved in building up a research group in underwater technology and maritime robotics with KTH and is currently a PI of the Swedish Maritime Robotics Centre (SMaRC) hosted by KTH that involves research on underwater robotics.

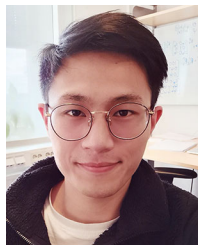

Tianlei Miao (Member, IEEE) received the bachelor's degree in naval architecture and ocean engineering from Zhejiang University, Hangzhou, China, in 2017, and a joint master's degree in maritime engineering from the Norwegian University of Science and Technology (NTNU), Trondheim, Norway, and the Royal Institute of Technology (KTH), Stockholm, Sweden, in 2019.

He is currently working on the Marie Skłodowska-Curie actions ETN-SAS project as an early-stage Researcher cooperated with both KU Leuven, Leuven, Belgium, and RH Marine, Schiedam, The Netherlands. His research interests include data fusion, multiobject tracking, motion prediction, and collision avoidance in the autonomous vessels field.